Modeling and control of a 4-ADOF upper-body exoskeleton with mechanically decoupled 3-D compliant arm-supports for improved-pHRI

Nauman Masud [a,b,*], Dario Senkic [c], Christian Smith [b], Magnus Isaksson [a]

[a] Department of Electrical Engineering, Mathematics, and Science, University of Gävle, 80176, Sweden
[b] Department of Robotics, Perception, and Learning, Royal Institute of Technology, Stockholm, 100 44, Sweden
[c] Department of Industrial Design, Management and Mechanical Engineering, University of Gävle, 80176, Sweden

ABSTRACT

Safe physical human-robotic interaction is a crucial concern for worn exoskeletons where lower weight requirement limits the number and size of actuators to be used. A novel control strategy is suggested in this paper for the low degree of freedom exoskeletons, by combining proposed mechanically decoupled passive-compliant arm-supports with active compliance, to achieve an improved and safer physical-human-robotic-interaction performance, while considering the practical limitations of low-power actuators. The approach is further improved with a novel vectoral-form of disturbance observer-based dynamic load-torque compensator, proposed to linearize and decouple the nonlinear human-machine dynamics effectively. The design of a four-degree of freedom exoskeleton test-rig that can assure the implementation of the proposed strategy is also shortly presented. It is shown through simulation and experimentation, that the use of proposed strategy results in an improved and safer physical human-robotic interaction, for the exoskeletons using limited-power actuators. It is also shown both through simulation and experimentation, that the proposed vectoral-form of disturbance based dynamic load-toque compensator, effectively outperforms the other traditional compensators in compensating the load-torques at the joints of the exoskeleton.

1. Introduction

An increase in the average lifespan of a human has led to active research in the field of assistive exoskeletons, which in contrast to rehabilitation exoskeletons, have to be worn by the user to assist in his daily activities and hence its weight is of prime consideration. This means a lower actuator count, which in turn implies a lower active degree of freedom (LADOF). A LADOF exoskeleton not only is a requirement for reducing human fatigue but also for a longer battery life of the mobile assistive exoskeleton devices. A number of upper-limb exoskeletons with high active degree of freedom (ADOF) such as 6-ADOF and above have been developed [1–7], but are generally designed for rehabilitation applications and are fixed and not meant to be carried by humans because of their considerable weight. On the other hand, low active degree of freedom exoskeletons (ADOF < 6) also exist but are limited in either assisting the human along all the task-space direction at the point of contact [8–10], or they are cumbersome like ARMMin-III [11–13]. Research in the LADOF robotic manipulators has hence gained importance from the perspective of developing assistive devices, which are light and can provide adequate assistance to the user

in performing their normal daily activities in spite of being less dexterous as compared to the high degree of freedom exoskeletons [14, 15]. It is therefore desired that both the design and control methodologies be investigated and analyzed for LADOF exoskeletons, which can not only assist the human in the same way as their higher DOF counterparts but also ensure stable, safe and harmonious physical-human robot interaction (pHRI).

The limited power actuators used in wearable exoskeletons suffer from high impedance due to the reflected moment of inertia and low force tracking bandwidth. These actuators, therefore, act as poor force sources and hence are not safe to be used in pHRI based assistive applications as such [16,17]. The limitation of actuators as a poor source of force can be mitigated by the use of RSEAs [18–20]. The RSEAs are generally used under active force feedback control at the joint level. The serial compliant element in the RSEAs can effectively decouple the dynamics of the actuator from that of the load, allowing for much better control of the actuator [21]. In exoskeleton applications, where the exoskeleton acts as a serial manipulator, RSEAs have their limitations. Firstly, the joint stiffness of the RSEAs cannot be increased beyond the stiffness of the series compliant spring without compromising the
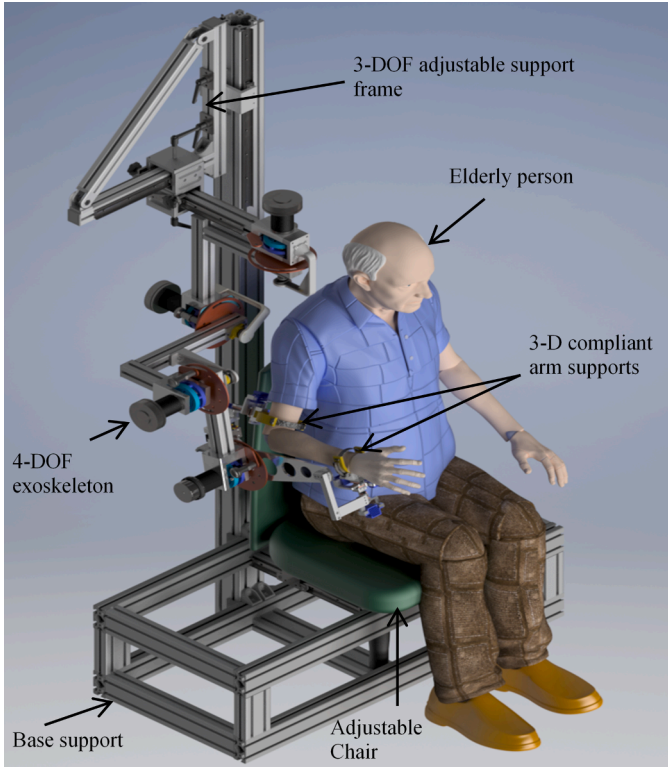
Fig. 1. Developed 4-ADOF arm-exoskeleton test-rig.

passive stability of the respective RSEA [21]. Secondly, the reflected mass of the exoskeleton would severely limit the achievable bandwidth of the RSEAs [21]. Lastly, controlling the impedance of the RSEAs as in [21,22] at each joint does not straightforwardly imply controlling the end-point task-space impedance of the exoskeleton. Though this can be done but would require additional complex control structures, therefore, safe end-point pHRI performance cannot be assured by the use of RSEAs alone at the joint-level.

The task-space pHRI, on the other hand, can also be made safe by the use of active compliance techniques such as impedance control [23,24]. Impedance-based control [25], has extensively been applied in the field of serial robotics, especially for ensuring safe-pHRI in industrial applications [26–28]. Assistive exoskeletons have also recently seen the implementation of impedance-based control strategies to ensure intrinsically safe human-exoskeleton interactions [29–33]. Active compliance techniques are adaptive, and the impedance of the device can easily be changed online, which is a very desirable feature for assistive devices. Nonetheless, as shown in Section 2, because of the rigid off-the-shelf force sensors, along with the high structural rigidity of the exoskeleton mechanical structure, it is challenging for the exoskeleton system using low-power actuators (with limited bandwidth) to impose the desired value of low impedance. This can then cause stability issues and hence, an unsafe-pHRI.

The human limb is intimately attached to the exoskeleton at the contact supports. Therefore, the nonlinear dynamics of the human is coupled to the nonlinear dynamics of an exoskeleton at the point of contact, which in turn effectively appear as uncertain-nonlinear load-torque at each joint actuator of the exoskeleton [34]. Furthermore, any uncertainty in exoskeleton kinematics and misalignment of the joint axis between human and exoskeleton adds to the uncertainty of these joint load-torques.

A novel combinational approach is suggested in this paper to achieve an improved and safer task-space pHRI performance of an exoskeleton. The strategy proposes to use the proposed new passive-compliant supports in combination with active impedance control for a 4-ADOF exoskeleton, as shown in Fig. 1. The suggested control approach is additionally combined with the novel vectoral-form of disturbance observer-based dynamic load torque compensator (DOB-based-DLTC) to further improve the pHRI performance by compensating the undesired nonlinear load-torques at all the joint-actuators of the exoskeleton. The proposed new approach is justified both theoretically and experimentally and is shown to limit the physical mechanical-impedance of the exoskeleton for a safer pHRI.

Limitations in providing safe-pHRI for an impedance-controlled LADOF-exoskeleton with single-support are first investigated in Section 2. Modeling for the proposed 4-ADOF arm-exoskeleton using the new passive-compliant supports is presented in Section 3. A novel control strategy using the proposed vectoral DOB-based-DLTC is then presented in Section 4 to ensure improved pHRI performance for the exoskeleton. The proposed control strategy is then validated for improved pHRI performance through simulation in Section 5 by using the developed human-exoskeleton model. The experimental setup for validating the empirical pHRI performance of the developed 4-ADOF exoskeleton is presented in Section 6. Experimental verification of the proposed novel control strategy for improved pHRI performance is then presented in Section 7 using the developed test-rig. The theoretical justification of using the suggested new passive-compliant arm supports for ensuring safe-pHRI of an exoskeleton under impedance-control is finally presented in Section 8.

2. Limitations of a single support LADOF-exoskeleton

To ensure safe-pHRI, the exoskeleton is expected to have a certain desired level of active compliance, which can be ensured by controlling the exoskeleton under task-space impedance control. An impedance controlled LADOF exoskeleton using a traditional six-dimensional (6-D) force sensor at the arm support alone suffers from several aspects. To ascertain these limitations, an impedance control law for the 4-ADOF exoskeleton is derived in (B.10,B.12) in Appendix B, and it is seen that the angular task-space position error $\mathbf{e}_{\omega_{la}}$ and its derivatives $\dot{\mathbf{e}}_{\omega_{la}}, \ddot{\mathbf{e}}_{\omega_{la}}$ are not straight forward to compute. The singularity condition for matrix $\boldsymbol{L}$ in (B.6) in Appendix B must always be met to avoid computational singularity in computing $\dot{\mathbf{e}}_{\omega_{la}}$ and $\ddot{\mathbf{e}}_{\omega_{la}}$. Furthermore, it is shown in (B.14) in Appendix B that the reference joint-space acceleration $\ddot{q}_r$, is only available as a least square solution. This can affect the accurate tracking of reference task-space acceleration of the arm support $\ddot{\mathbf{x}}_{r_{la}}$ and hence, can limit the accuracy of achievable desired-impedance (defined in Appendix B) of the exoskeleton. Also, the sensed forces along different directions from a 6-D sensor must be decoupled using calibration and the decoupling matrix, each time after sensing, which in turn increases the computational load. Lastly, the available 6-D sensors are very rigid. With a rigid exoskeleton mechanical structure and the human arm intimately attached to the exoskeleton at the contact support, any small misalignment between the human arm and the exoskeleton over the course of movement would result in large interactive forces. This consequently would require huge reference accelerations ($\ddot{\mathbf{x}}_{r_{la}}$) in task-space and therefore in joint-space ($\ddot{q}_r$), to impose the desired end-point impedance at the lower-arm support. These accelerations would be very difficult to track in practice due to saturation and bandwidth limitation of the exoskeleton actuators with limited power, size, and weight. This
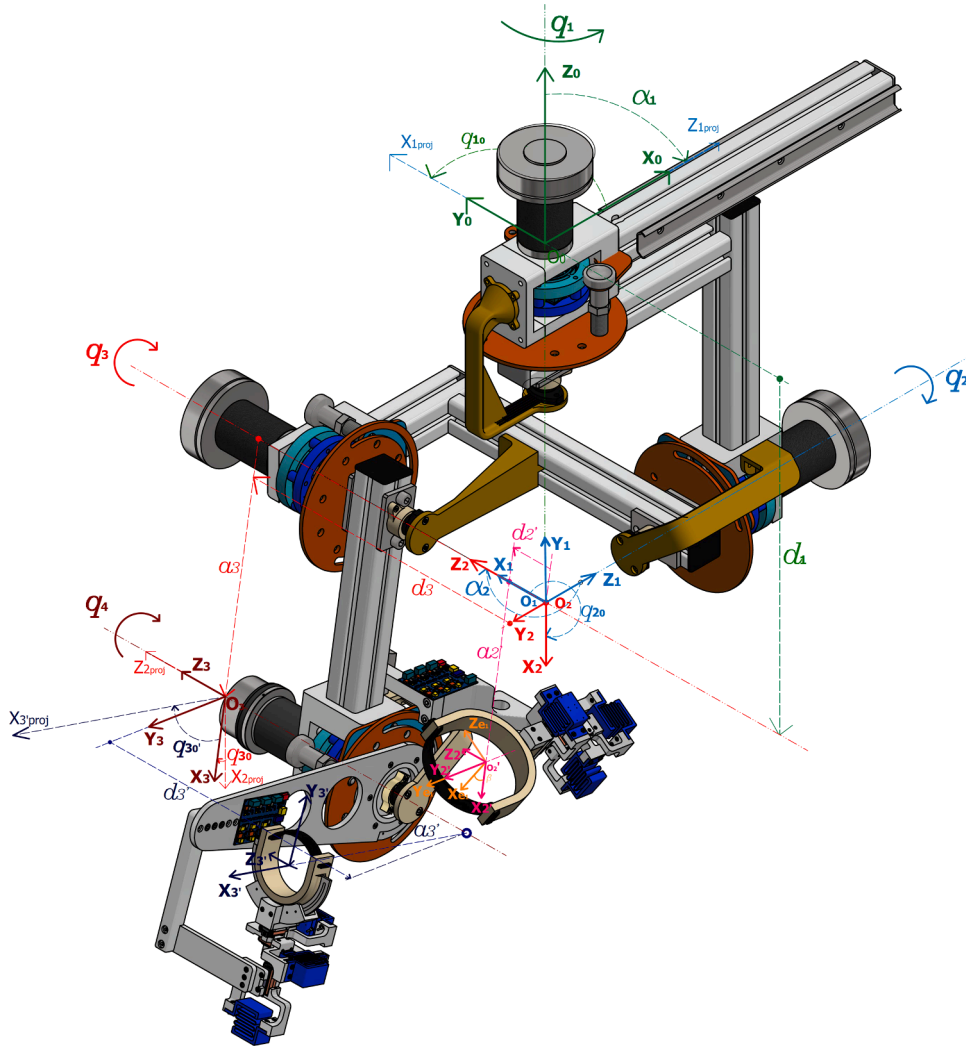
Fig. 2. Frame definition for the 4-ADOF arm exoskeleton.

Table 1
D-H frame definitions with associated joint angles.

Frame	Description	Joint angle
Σ_0	Base-frame: $O_0 - X_0 Y_0 Z_0$	q_1 (shoulder supination)
Σ_1	Link-1 frame: $O_1 - X_1 Y_1 Z_1$	q_2 (shoulder abduction/adduction)
Σ_2	Link-2 frame: $O_2 - X_2 Y_2 Z_2$	q_3 (shoulder extension/flexion)
Σ_2'	Upper-arm support frame $O'_2 - X'_2 Y'_2 Z'_2$	without β* rotation
Σ_{ua}	Upper-arm support frame: $O'_2 - X_{e_l} Y_{e_l} Z_{e_l}$	with β* rotation
Σ_3	Link-3 frame: $O_3 - X_3 Y_3 Z_3$	q_4 (elbow extension/flexion)
Σ_{la}	Lower-arm support frame: $O'_3 - X'_3 Y'_3 Z'_3$	

* β is defined in Table A-1.

sequentially would result, in a poor desired- impedance tracking at the contact support of the exoskeleton, which would further increase the interactive forces and create stability problems. It is, therefore, challenging to ensure a safe-pHRI for an impedance controlled LADOF arm-exoskeleton, using a rigid 6-D force sensor at the lower-arm support alone with limited power actuators.

3. Exoskeleton modelling

To overcome the limitations of a single support LADOF-exoskeleton, a new 4-ADOF-exoskeleton with two novel passive-compliant arm-supports is suggested. For the proper analysis of the proposed exoskeleton, the kinematic and dynamic modeling of the exoskeleton is first presented.

3.1. Kinematic modeling

The human-arm interacts intimately with the exoskeleton at the arm-supports. Therefore, kinematics for both upper and lower-arm supports need to be accurately found for correct estimation of their respective task-space positions, velocities, and accelerations. The designed arm-exoskeleton, along with the defined reference-frames as per Denavit Hartenberg (D-H) convention, is shown in Fig. 2. Reference-frames and the associated joint angles are described in Table 1, while the corresponding D-H parameters are listed in Table A1 in Appendix A. If q_{m_1}, q_{m_2}, q_{m_3} and q_{m_4} are the measured joint angles, then the joint angle vector $\mathbf{q} \in \mathbb{R}^4$ is defined as

$$\mathbf{q} = [q_1 q_2 q_3 q_4]^T, \tag{1}$$

where

$$q_1 = q_{m_1} + q_{0_1}, \quad q_2 = q_{m_2} + q_{0_2},$$

$$q_3 = q_{m_3} + q_{0_3}, \quad q_4 = q_{m_4} + q'_{0_3}.$$

Here $q_{1_0}, q_{2_0}, q_{3_0}$ and q'_{3_0} are the associated joint-angle offsets and listed in Appendix A. The two arm-supports of the exoskeleton, i.e., the upper-arm support and the lower-arm support can be considered as two end-effectors of a serial manipulator having 3-DOF and 4-DOF respectively. Therefore, homogenous transformations $T_{ua}(q), T_{la}(q) \in \mathbb{R}^{4 \times 4}$ and Jacobian matrices $J_{ua}(q), J_{la}(q) \in \mathbb{R}^{6 \times 4}$ for respective upper and lower-arm supports, are found with respect to (w.r.t) base-frame $\sum_0$. The interactive forces ($\mathbf{f}^e_{h_{ua}}, \mathbf{f}^e_{h_{la}}$) at the two arm supports are measured in their respective support frames; therefore, the end-effector Jacobian matrices $J^e_{ua}(q), J^e_{la}(q) \in \mathbb{R}^{6 \times 4}$ w.r.t to respective frames $\sum_{ua}$ and $\sum_{la}$ have also been found. This allows for a direct transformation between the measured forces on the human-arm ($\mathbf{f}^e_{h_{ua}}, \mathbf{f}^e_{h_{la}}$) and the corresponding interactive torques ($\tau_{h_{ua}}, \tau_{h_{la}}$), produced at the joints of the exoskeleton as shown in Appendix A.

3.2. Dynamics of human-exoskeleton system

Human and exoskeleton interact with each other at the two arm-supports, therefore, the joint load-torque $\tau_L \in \mathbb{R}^4$ for the 4-ADOF exoskeleton is given by the forward dynamic equation of the human-exoskeleton system as [34].

$$\tau_L = \mathbf{M}_{la}(\mathbf{q})\ddot{\mathbf{q}} + \mathbf{C}_{la}(\mathbf{q}, \dot{\mathbf{q}})\dot{\mathbf{q}} + \mathbf{g}_{la}(\mathbf{q}) + \tau_{h_{ua}} + \tau_{h_{la}}. \tag{2}$$

Where q is the joint angle vector defined in (1), $\mathbf{M}_{la}(q), \mathbf{C}_{la}(q, \dot{q}) \in \mathbb{R}^{4 \times 4}$ are the respective Mass and Coriolis matrices at the lower-arm support and $\mathbf{g}_{la}(q) \in \mathbb{R}^4$ is the gravity vector found using the respective transformations (A.1-A.3) and the inertial-parameters listed in Table A2 in Appendix A. The torques $\tau_{h_{ua}}, \tau_{h_{la}}$ in (2) are the interactive joint torques due to corresponding forces on the human-arm at the upper and lower-arm supports. The uncertain non-linear dynamics of the human-arm is, therefore, linked to the dynamics of the exoskeleton, through the interactive forces ($\mathbf{f}^e_{h_{ua}}, \mathbf{f}^e_{h_{la}}$) at the two arm-supports.

4. Control strategy

The pHRI of an exoskeleton can be improved by the use of passive-compliant elements alone at the arm supports [16,35], but this would then fix the apparent impedance of the exoskeleton that cannot be changed or controlled. However, for an exoskeleton under active impedance control, the use of a serial passive compliance element in combination can improve not only the system stability but also the fidelity of the force feedback system [36]. This results in lower interactive forces and hence a better pHRI, as shown in Section 5 and Section 8.

4.1. Impedance control of 4-ADOF arm-exoskeleton with 3-D passive arm supports using resolved acceleration control

To improve the impedance control performance of the exoskeleton, two novel passive-compliant arm supports are suggested. These supports are suggested to be at the upper and lower-arm positions, as shown in Fig. 1. Both the arm-supports, in contrast to the rigid traditional 6-D force sensor, are designed to not only offer a mechanically decoupled 3-D passive-compliance but also be able to sense each component of 3-D interactive forces independently. The suggested supports are shown in detail in Fig. 14. Since each component of interactive forces is independently sensed, no software decoupling is required. As the sensed forces $\mathbf{f}^e_{h_{ua}}, \mathbf{f}^e_{h_{la}}$ on the human at the respective arm-supports are only three dimensional (with no moment sensing), only the linear

components of task-space positions, velocities, and accelerations ($\in \mathbb{R}^3$) of the arm supports can be controlled. These terms can hence be written from Appendix A and Appendix B as

$$\mathbf{x}_{la} = \mathbf{x}_{v_{la}}, \qquad\qquad \mathbf{x}_{d_{la}} = \mathbf{x}_{d_{v_{la}}},$$
$$\ddot{\mathbf{x}}_{d_{la}} = \ddot{\mathbf{x}}_{d_{v_{la}}}, \qquad\qquad \mathbf{e}_{la} = \mathbf{e}_{v_{la}} = \mathbf{x}_{d_{la}} - \mathbf{x}_{la},$$
$$\mathbf{e}_{la} = \dot{\mathbf{e}}_{v_{la}}, \qquad\qquad \ddot{\mathbf{e}}_{la} = \ddot{\mathbf{e}}_{v_{la}},$$
$$\mathbf{f}_{h_{la}} = \mathbf{f}_{h_{v_{la}}}, \qquad\qquad \mathbf{f}_{h_{ua}} = \mathbf{f}_{h_{v_{ua}}},$$
$$\mathbf{f}^e_{h_{la}} = \mathbf{f}^e_{h_{v_{la}}}, \qquad\qquad \mathbf{f}^e_{h_{ua}} = \mathbf{f}^e_{h_{v_{ua}}},$$
$$\mathbf{x}_{la} = \dot{\mathbf{x}}_{v_{la}} = \mathbf{J}_{v_{la}}(\mathbf{q})\dot{\mathbf{q}},$$
$$\ddot{\mathbf{x}}_{la} = \ddot{\mathbf{x}}_{v_{la}} = \mathbf{J}_{v_{la}}(\mathbf{q})\ddot{\mathbf{q}} + \dot{\mathbf{J}}_{v_{la}}(\mathbf{q})\dot{\mathbf{q}},$$
$$\tau_{h_{la}} = \mathbf{J}^e_{v_{la}}(q)^T\mathbf{f}^e_{h_{la}}, \tau_{h_{ua}} = \mathbf{J}^e_{v_{ua}}(\mathbf{q})^T\mathbf{f}^e_{h_{ua}}. \tag{3}$$

Where $\mathbf{J}_{v_{la}}(\mathbf{q}) \in \mathbb{R}^{3 \times 4}$ is the velocity Jacobian w.r.t frame $\sum_o$, while $\mathbf{J}^e_{v_{ua}}(\mathbf{q})$, $\mathbf{J}^e_{v_{la}}(\mathbf{q}) \in \mathbb{R}^{3 \times 4}$ are the respective velocity Jacobians w.r.t respective frames $\sum_{ua}$ and $\sum_{la}$. Vectors $x_{dla}, \ddot{x}_{d_{la}}$ in (3)[1] are the respective task-space desired position and acceleration of the lower-arm support. The desired-impedance for the lower-arm support can hence only be linear as defined in (B.10) in Appendix B. Therefore, the reference task-space acceleration required to ensure the desired-impedance is also linear i.e. $\ddot{\mathbf{x}}_{r_{la}} = \ddot{\mathbf{x}}_{r_{v_{la}}} \in \mathbb{R}^3$ and is given from (3) and Appendix B as

$$\ddot{\mathbf{x}}_{r_{la}} = \ddot{\mathbf{x}}_{d_{la}} - \mathbf{M}^{-1}_{v_d}\left(\mathbf{f}_{h_{la}} - \mathbf{B}_{v_d}\dot{\mathbf{e}}_{la} - \mathbf{K}_{v_d}\mathbf{e}_{la}\right). \tag{4}$$

Where Matrices $\mathbf{M}_{v_d}$, $\mathbf{B}_{v_d}$ and $\mathbf{K}_{v_d}$ are the desired linear impedance matrices defined in Appendix B. Here $j = 1$ to 3 and $m_{v_{d_j}}, b_{v_{d_j}}$ and $k_{v_{d_j}}$ are the respective linear desired task-space parameters for mass, damping, and stiffness. The corresponding reference joint-space acceleration $\ddot{q}_r \in \mathbb{R}^4$ is then given in terms of lower-arm support Jacobian from (3) and (4) as

$$\ddot{\mathbf{q}}_r = \mathbf{J}_{v_{la}}(\mathbf{q})^{\dagger}\left(\ddot{\mathbf{x}}_{r_{la}} - \dot{\mathbf{J}}_{v_{la}}(\mathbf{q})\dot{\mathbf{q}}\right), \tag{5}$$

where + represents the pseudo inverse. The Eq. (5) here is under-determined and hence possess infinite many exact solutions for the reference joint-space acceleration $\ddot{q}_r$. As clear from (5), simultaneous control of both the task-space position and orientation of the lower-arm support for a 4-ADOF exoskeleton with a 3-D force sensor is not possible, as 1-DOF is uncontrolled, which if not regulated could cause discomfort to the human at the upper-arm. It is therefore suggested that the remaining 1-DOF be regulated by controlling the upper-arm support in the null-space of the lower-arm support Jacobian $\mathbf{J}_{v_{la}}(\mathbf{q})$, so that the impedance control performance of the lower-arm is not affected.

If $\mathbf{f}^e_{h_{d_{ua}}} \in \mathbb{R}^3$ is the desired interactive forces on the human at the upper-arm support in the frame $\sum_{ua}$, then it is desired that $\mathbf{f}^e_{h_{d_{ua}}}$ be zero so that the upper-arm support appears transparent to the user in any direction. Using a proportional force-controller $\mathbf{K}_f$, the modulating force $\mathbf{f}^e_{\xi_{ua}}$ for upper-arm support in the frame $\sum_{ua}$ is therefore given by $\mathbf{f}^e_{\xi_{ua}} = \mathbf{K}_f(\mathbf{f}^e_{h_{d_{ua}}} - \mathbf{f}^e_{h_{ua}})$. The null-space torque $\tau_{\xi_{ua}}$ corresponding to force $\mathbf{f}^e_{\xi_{ua}}$ is hence given as

$$\tau_{\xi_{ua}} = \mathbf{J}^e_{v_{ua}}(\mathbf{q})^T\mathbf{f}^e_{\xi_{ua}} = \mathbf{J}^e_{v_{ua}}(\mathbf{q})^T\mathbf{K}_f\left(\mathbf{f}^e_{h_{d_{ua}}} - \mathbf{f}^e_{h_{ua}}\right), \tag{6}$$

where force-controller $\mathbf{K}_f = diag\{k_{f_i}\}$ for i=1 to 3. For $\ddot{\mathbf{x}}_{r_{la}}$ given by (1), the reference joint-space acceleration $\ddot{q}_r$ with null-space force control of the upper-arm support is then suggested to be given from (2) as

---

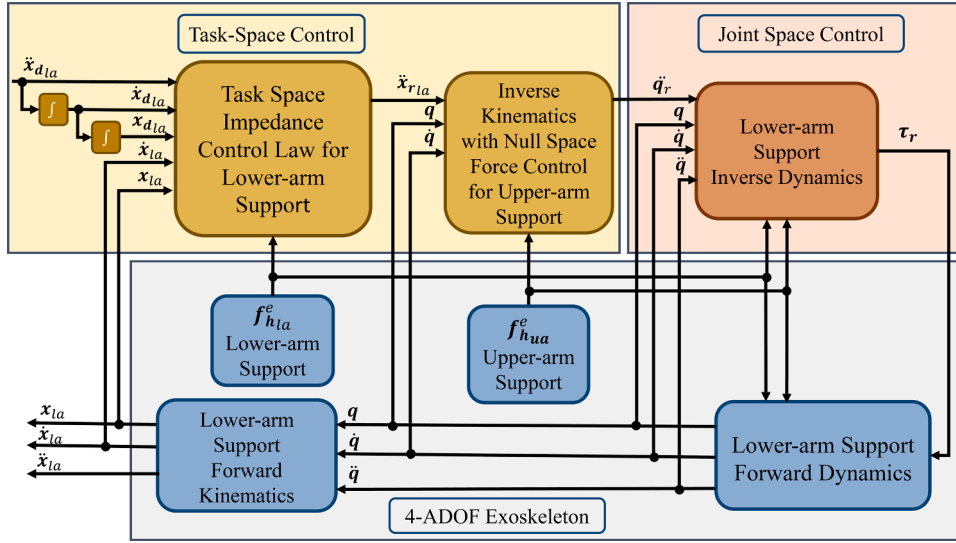[1] The subscript 'v' in (3) represent linear quantities.

Fig. 3. Lower-arm support impedance control strategy for 4-ADOF arm-exoskeleton with null space force control of upper-arm support using resolved acceleration control.

$$\ddot{\mathbf{q}}_r = \mathbf{J}_{v_{la}}(\mathbf{q})^{+}\left(\ddot{\mathbf{x}}_{r_{la}} - \dot{\mathbf{J}}_{v_{la}}(\mathbf{q})\dot{\mathbf{q}}\right) + \left(\mathbf{I} - \mathbf{J}_{v_{la}}(\mathbf{q})^{+}\mathbf{J}_{v_{la}}(\mathbf{q})\right)\boldsymbol{\xi}, \tag{7}$$

where $\boldsymbol{\xi} \in \mathbb{R}^4$ is the null-space acceleration vector for the null-space force control of the upper-arm support and is proposed to be given as

$$\boldsymbol{\xi} = \mathbf{M}_{\xi_{ua}}^{-1}(\boldsymbol{\tau}_{\xi_{ua}} - \mathbf{B}_{\xi_{ua}}\dot{\mathbf{q}}). \tag{8}$$

The null-space dynamics in (7) is dictated by the respective diagonal mass and damping matrices $\mathbf{M}_{\xi_{ua}}$ and $\mathbf{B}_{\xi_{ua}} \in \mathbb{R}^{4 \times 4}$, whereas $\boldsymbol{\tau}_{\xi_{ua}}$ in (8)(8) is given by (6). For $\ddot{\mathbf{q}}_r$ given by (7), the reference torque $\boldsymbol{\tau}_r \in \mathbb{R}^4$ required for compensating the human-exoskeleton dynamics in (2), is given as

$$\boldsymbol{\tau}_r = \widehat{\mathbf{M}}_{la}(\mathbf{q})\ddot{\mathbf{q}}_r + \widehat{\mathbf{C}}_{la}(\mathbf{q},\dot{\mathbf{q}})\dot{\mathbf{q}} + \widehat{\mathbf{g}}_{la}(\mathbf{q}) + \boldsymbol{\tau}_{h_{la}} + \boldsymbol{\tau}_{h_{ua}}, \tag{9}$$

where $\widehat{M}_{la}(q)$, $\widehat{C}_{la}(q,\dot{q})$ and $\widehat{g}_{la}(q)$ are respective estimates of $M_{la}(q)$,

$C_{la}(q,\dot{q})$ and $g_{la}(q)$ in (2). With ideal estimates and with ideal actuator dynamics, computed reference torque τ_r in (9) is precisely equal to the actual load-torque τ_L in (2). Hence the actual joint-acceleration $\ddot{q}$ accurately tracks the reference acceleration which in-turn ensures that the actual task-space acceleration of the lower-arm support $\ddot{x}_{la}$ given by (3) accurately tracks the reference acceleration $\ddot{x}_{r_{la}}$ dictated by the impedance control law in (4). The null-space based impedance control strategy for two compliant supports under ideal load-torque compensation is shown in Fig. 3. The exoskeleton, therefore, has the desired-impedance response at the lower-arm support while at the same time, the force at the upper-arm support is regulated in the null-space of lower-arm support Jacobian. This ensures that the complete pose of the exoskeleton is controlled without degrading the impedance control performance of the lower-arm support by requiring an easily computable linear error vector $\mathbf{e}_{la} = \mathbf{e}_{v_{la}}$ and its derivatives. Since there is no
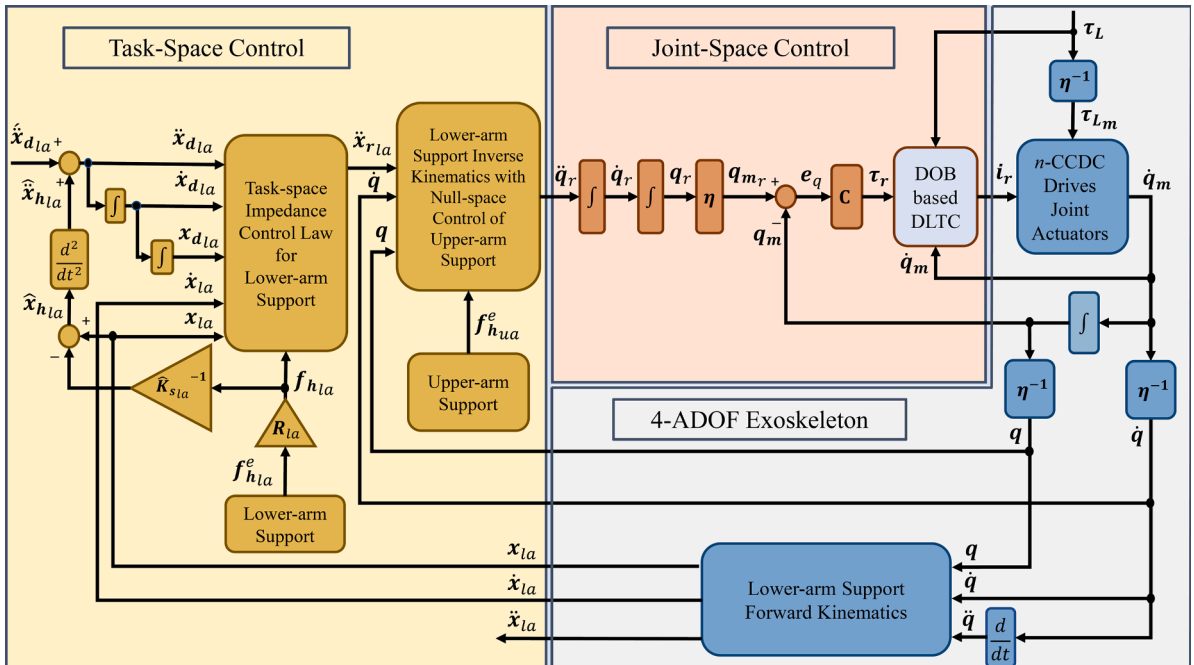

Fig. 4. Impedance control strategy for a 4-ADOF arm-exoskeleton with two passive-compliant arm-supports using DOB-based-DLTC.
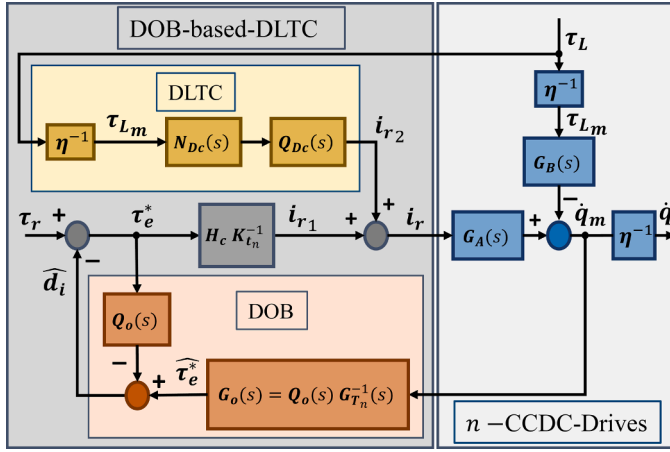
Fig. 5. Detailed structure of the proposed DOB-based-DLTC in vectorial form for n-CCDC-drives.

Fig. 6. Block diagram of a CCDC-drive at j_{th} joint of the arm-exoskeleton.

need to compute the angular error vector $\mathbf{e}_{\omega_{la}}$ and its derivatives, the computational singularity problems associated with it (as mentioned in Section 2), are avoided. Furthermore, the solution for joint reference acceleration $\ddot{\mathbf{q}}_r$ is obtained in (7) as an exact solution instead of a least square solution, ensuring an accurate computation of $\ddot{\mathbf{q}}_r$, which in-turn improves the tracking performance of $\ddot{x}_{la}$ and hence, the impedance control response.

4.2. Limitations of resolved acceleration control

Though, the impedance control strategy, as shown in Fig. 3 for the 4-ADOF arm-exoskeleton using resolved acceleration control looks promising; it has certain practical shortcomings. Firstly, due to the relatively large size of the forward dynamics matrix estimates $\widehat{M}_{la}(\mathbf{q})$, $\widehat{C}_{la}(\mathbf{q},\dot{\mathbf{q}})$ and $\widehat{g}_{la}(\mathbf{q})$ in (9), with multiplicative sinusoidal terms of $\mathbf{q}$, the computation of these matrices is time-intensive. Therefore, it can significantly increase sample-time in real-time applications. Secondly, due to inevitable errors in these matrix estimates, the computed reference torque τ_r in (9) would differ from the actual torque τ_L. Therefore, the exoskeleton system in (2) would not be fully linearized. Thirdly, the task and joint-space control laws, given by (4) and (5), suffer from a lack of initial conditions. Therefore, any error in position or velocities due to their initial values in task-space or joint-space would never be compensated. Furthermore, it is imperative for the proper estimation of the gravity vector $\widehat{g}_{la}(\mathbf{q})$ in (9), to accurately know the angle, the gravity plane makes with the base-frame $\sum_0$. With a fixed base-frame, as shown in (9) this angle is zero, but it is not always the case for worn exoskeleton as this angle would vary with the human spine and torso movement. Additional sensors are hence required to estimate this angle. Without proper sensing of this angle, the estimate $\widehat{g}_{la}(\mathbf{q})$ can give very erroneous results for worn exoskeletons.

4.3. Proposed impedance control strategy for the 4-ADOF arm-exoskeleton with two passive-compliant arm-supports using DOB-based-DLTC

To further improve the impedance control performance, it is suggested firstly, to sense the joint load-torques directly for all the active joints of the exoskeleton using joint torque sensors. Secondly, to use current-controlled DC-drives (CCDC-drives) as joint-actuators for their inherent superior torque performance [37,38]. Thirdly, to employ the proposed vectorial-form of disturbance observer-based dynamic load torque compensator (DOB-based-DLTC) technique to effectively compensate the uncertain load-torques τ_L, so as to linearize and decouple the joint-space dynamics of the human-arm-exoskeleton
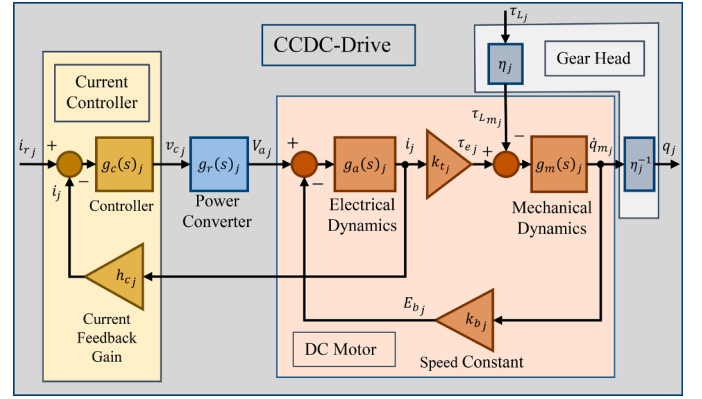
system in (2).

The proposed control strategy is shown in Fig. 4. The strategy mainly consists of a task-space impedance control law for the lower-arm support, a joint-space control law with null-space force control for the upper-arm support, a joint-level position controller, and the proposed vectorial form of DOB-based-DLTC for the four CCDC-drives of the exoskeleton. It is shown in [39] that there exists stability vs. accuracy dilemma in practically achieving the desired level of end-point impedance. Accurate implementation of impedance control requires accurate tracking of joints-space reference acceleration $\ddot{\mathbf{q}}_r$ which is difficult to achieve in practice with stability. On the other hand, position reference tracking in joint-space is possible with sufficient stability, but it introduces integration lag and hence deteriorates the accuracy of achieved end-point impedance, which in turn result in higher human-interactive forces. A position form of impedance control is therefore selected for implementation for maximum stability [24,40], and it is investigated as to how well the complaint arm-support at the lower-arm can mitigate the effect of this lag and reduce the undesired human-interactive force.

4.3.1. Proposed vectorial form of DOB-based-DLTC

In a recent work, a disturbance observer-based dynamic load torque compensator (DOB-based-DLTC) was implemented for a single joint to compensate for the uncertain-nonlinear joint load-torque [34]. If this technique is applied to all the n active joints of the exoskeleton ($n = 4$), it can effectively linearize and decouple the human-exoskeleton system in (2), allowing linear and decoupled joint-level controllers to be designed independently [34].

Detail structure of the proposed DOB-based-DLTC in its vectorial form is shown in Fig. 5 whereas a detailed block diagram for a CCDC-drive at the j_{th} joint ($j = 1$ to 4) is shown in Fig. 6. All the transfer functions and gains in Fig. 6 have been defined in detail in [34] where as all the parameters for the j_{th} CCDC-drive are defined in Table C1, Table C2 and Table C3 in Appendix C. To model the CCDC-drive accurately, the dynamics of all its components have been considered. If $\mathbf{i}_r \in \mathbb{R}^4$ is the reference-current-control-input in volts, $\tau_L \in \mathbb{R}^4$ is the sensed load-torque at the output shafts of all the joints and $\dot{\mathbf{q}} \in \mathbb{R}^4$ is the output angular velocity vector, then an accurate frequency domain vectorial model for the n-CCDC-drives can be derived in terms of its inputs $\mathbf{i}_r$ and τ_L as [34].

$$\dot{\mathbf{q}} = \boldsymbol{\eta}^{-1}\mathbf{G}_{A_n}(s)\,\mathbf{i}_r - \left(\boldsymbol{\eta}^2\right)^{-1}\mathbf{G}_{B_n}(s)\,\tau_L \,, \tag{10}$$

where $\mathbf{G}_{A_n}(s)$ and $\mathbf{G}_{B_n}(s)$ are the diagonal transfer function matrices defining the nominal dynamics from $\mathbf{i}_r$ to $\dot{\mathbf{q}}$ and τ_L to $\dot{\mathbf{q}}$ respectively, for the nominal drive parameters in Table C1-Table C3 in Appendix C. Matrix $\boldsymbol{\eta}$ is the diagonal gear-ratio matrix for the n-CCDC-drives. Matrices $\mathbf{G}_{A_n}(s)$, $\mathbf{G}_{B_n}(s)$ and $\boldsymbol{\eta}$ are hence defined as

$$\mathbf{G}_{A_n}(s) = diag\left\{g_{A_n}(s)_j\right\}, \quad \mathbf{G}_{B_n}(s) = diag\left\{g_{B_n}(s)_j\right\}, \quad \boldsymbol{\eta} = diag\left\{\eta_j\right\}. \tag{11}$$

where $j = 1$ to 4. If $g_c(s)_j$, $g_r(s)_j$ and $g_a(s)_j$ are the respective transfer functions for the current-controller, power-converter, and electrical-dynamics of the j_{th} CCDC-drive in Fig. 6, then the corresponding transfer functions $g_{A_n}(s)_j$ and $g_{B_n}(s)_j$ in (11) can be defined in terms of the nominal parameters of CCDC-drive, as shown in (C.1) in Appendix C [34].

To effectively cancel the sensed load torque τ_L in (10), the dynamic load-torque compensator (DLTC) $\boldsymbol{N}_{Dc}(s)$ for the n-CCDC-drives in Fig. 5 is defined in vectoral form (11) as [34]

$$\mathbf{N}_{Dc}(s) = diag\{n_{Dc}(s)_j\}, \tag{12}$$

where

$$n_{Dc}(s)_j = \frac{i_{r2_j}}{\tau_{L_{m_j}}} = \frac{g_{B_n}(s)_j}{g_{A_n}(s)_j} \ , \ \text{for } j = 1 \text{ to } 4.$$

An explicit expression for $n_Dc(s)_j$ in (12) can be found in terms of the nominal parameters of the CCDC-drive as shown in (C.2) in Appendix C. Since $n_Dc(s)_j$ is improper with a degree of four, a diagonal filter matrix $\boldsymbol{Q}_{Dc}(s)$ of order larger than four is required for the proper realization of $\boldsymbol{N}_{Dc}(s)$ in (12). $\boldsymbol{Q}_{Dc}(s)$ is therefore defined as

$$\mathbf{Q}_{Dc}(s) = diag\{q_{Dc}(s)_j\}, \tag{13}$$

where

$$q_{Dc}(s)_j = \frac{\left(\left(\frac{1}{0.98\omega_{c_j}}\right)s + 1\right)}{\left(\left(\frac{1}{\omega_{c_j}}\right)s + 1\right)^6}, \ \text{for } j = 1 \text{ to } 4.$$

A realizable DLTC $N_{Dc_f}(s)$ is hence defined from (12) and (13) as

$$\mathbf{N}_{Dc_f}(s) = \mathbf{N}_{Dc}(s)\mathbf{Q}_{Dc}(s) = diag\{n_{Dc}(s)_j q_{Dc}(s)_j\} \ . \tag{14}$$

The cut-off frequency ω_{c_j} for each filter in (13) and sampling time t_s has to be carefully selected so as not to disturb the dominant dynamics of the respective $n_Dc(s)_j$ [34].

A realizable disturbance observer (DOB) that can give an estimate of the input disturbance $\widehat{\mathbf{d}}_i$ in Fig. 5 is given by

$$\widehat{\mathbf{d}}_i = \mathbf{G}_o(s)\boldsymbol{\eta}\dot{\boldsymbol{q}} - \mathbf{Q}_o(s)\boldsymbol{\tau}_e^*, \tag{15}$$

where $\boldsymbol{G}_o(s) \in \mathbb{R}^{4\times4}$ is given by

$$\mathbf{G}_o(s) = \mathbf{Q}_o(s)\mathbf{G}_{T_n}^{-1}(s). \tag{16}$$

Here matrix $\mathbf{G}_{T_n}(s)$ gives the nominal forward torque dynamics from τ_e^* to $\dot{q}$ and matrix $\boldsymbol{Q}_o(s)$ is the cascaded low pass filter matrix for proper implementation of DOB. The transfer function matrices $\mathbf{G}_{T_n}(s)$ and $\boldsymbol{Q}_o(s)$ in (16) are given as [34].

$$\begin{aligned} \mathbf{G}_{T_n}(s) &= diag\{ g_{T_n}(s)_j\}, \\ \mathbf{Q}_o(s) &= diag\{ q_o(s)_j\}, \end{aligned} \tag{17}$$

where

$$q_o(s)_j = 1.1 \ \omega_{oc_j}^2 \frac{\left(s + 0.9\omega_{oc_j}\right)}{\left(s + \omega_{oc_j}\right)^3} \ ,$$

for $j = 1$ to 4. The transfer function $g_{T_n}(s)_j$ in (17) is defined in terms of the nominal parameters of the CCDC-drive in (C.3) in Appendix C. To ensure closed-loop internal stability for the system in Fig. 5 with the DOB in feedback given by (15), the cut-off frequency ω_{oc_j} of the filter

$q_o(s)_j$ is choosen to be $0.2\omega_{n_j}$ [34], where ω_{n_j} is the bandwidth of the repective nominal forward system $g_{T_n}(s)_j$.

4.3.2. Decoupled joint-space controller

The joint-space position feedback control loop in Fig. 4 is required to ensure system robustness against initial value errors due to initial joint positions. If the load torque τ_L is accurately sensed, and the DOB-based-DLTC from (12) - (16) is properly implemented, the human-exoskeleton system in (2) would be effectively linearized and would only contain decoupled and well-defined linear-actuator-dynamics. This, in turn, would then allow for $n = 4$ independent linear joint-space position controllers to be designed for desired stability and robustness for the human-exoskeleton system [34]. The joint-space position controller $\boldsymbol{C}(s) \in \mathbb{R}^{4 \times 4}$ in Fig. 4 is, therefore, suggested to be given as

$$\mathbf{C}(s) = diag\{c(s)_j\}, \tag{18}$$

where

$$c(s)_j = \frac{k_{d_j}\left(\tau_{1_j}s + 1\right)}{\left(\tau_{2_j}s + 1\right)},$$

for $j = 1$ to 4. The PD controller $c(s)_j$ is designed using the corresponding nominal feedforward transfer function $g_{f_n}(s)_j = g_{T_n}(s)_j/s$.

4.3.3. Proposed control law

Both the proposed arm-supports for the exoskeleton are designed to have three mechanically decoupled passive-compliant elements (shown in detail in Fig. 14), therefore, the stiffness matrices $\boldsymbol{K}_{s_{la}}$, $\boldsymbol{K}_{s_{ua}}$, $\in \mathbb{R}^{3 \times 3}$ for the respective arm-supports are diagonal and are given by

$$\mathbf{K}_{s_{la}} = diag\left\{k_{s_{la_i}}\right\}, \quad \mathbf{K}_{s_{ua}} = diag\left\{k_{s_{ua_i}}\right\}. \tag{19}$$

Where $i=1$ to 3 and $k_{s_{la_i}}$, $k_{s_{ua_i}}$ are the respective stiffnesses of each compliant element for upper and lower-arm supports. The interactive forces on the human at these supports in the frame $\sum_o$ can hence be given in terms of stiffnesses of the compliant supports from (19) as

$$\begin{aligned} \mathbf{f}_{h_{la}} &= \mathbf{K}_{s_{la}}\left(\mathbf{x}_{la} - \mathbf{x}_{h_{la}}\right), \\ \mathbf{f}_{h_{ua}} &= \mathbf{K}_{s_{ua}}\left(\mathbf{x}_{ua} - \mathbf{x}_{h_{ua}}\right), \end{aligned} \tag{20}$$

where $\mathbf{x}_{h_{la}}$,$\mathbf{x}_{h_{ua}}$ are task-space positions of the human-arm at the upper and lower-arm contacts. To ensure that the apparent impedance at the lower-arm support along any i_{th} task-space direction never exceeds the stiffness of the respective compliant element $k_{s_{la_i}}$ as shown in detail in Section 8, the desired task-space position of the lower-arm support $\mathbf{x}_{d_{la}}$ is proposed to be given as

$$\mathbf{x}_{d_{la}} = \mathbf{x}''_{d_{la}} + \widehat{\mathbf{x}}_{h_{la}}, \tag{21}$$

where $\mathbf{x}''_{d_{la}} \in \mathbb{R}^3$ is the external desired input position and $\widehat{\mathbf{x}}_{h_{la}} \in \mathbb{R}^3$ is the estimated human lower-arm contact position in task-space. It follows from (19) and (20) that $\widehat{\mathbf{x}}_{h_{la}}$ can be estimated using measured interactive force $\mathbf{f}_{h_{la}}^e$ as

$$\widehat{\mathbf{x}}_{h_{la}} = \mathbf{x}_{la} - \left(\widehat{\mathbf{K}}_{s_{la}}\right)^{-1}\mathbf{f}_{h_{la}} = \mathbf{x}_{la} - \left(\widehat{\mathbf{K}}_{s_{la}}\right)^{-1}\mathbf{R}_{la} \ \mathbf{f}_{h_{la}}^e, \tag{22}$$

where $\widehat{\mathbf{K}}_{s_{la}}$ is the estimate of $\mathbf{K}_{s_{la}}$. For the interactive force $\mathbf{f}_{h_{la}}$ given by (20), the task-space impedance control law for the lower-arm support is defined by (4). To abide by the condition in (21), the desired task-space acceleration $\ddot{\mathbf{x}}_{d_{la}}$ in (4) is hence suggested to be given from (22) as

$$\ddot{\mathbf{x}}_{d_{la}} = \ddot{\mathbf{x}}''_{d_{la}} + \ddot{\widehat{\mathbf{x}}}_{h_{la}}, \tag{23}$$

where $\ddot{\mathbf{x}}''_{d_{la}}$ is the external desired input-acceleration for lower-arm support.

Therefore, for given desired external acceleration $\ddot{x}'_{d_{la}}$ and measured forces $\mathbf{f}^e_{h_{la}}$, $\mathbf{f}^e_{h_{ua}}$, the control law giving the reference joint-space acceleration $\ddot{q}_r$ (for the impedance controlled lower-arm support with null-space controlled upper-arm support), follows from (3), (4), (6), (7), (8), (22) and (23) as

$$\ddot{\mathbf{q}}_r = \mathbf{J}_{v_{la}}(\mathbf{q})^+ \left(\ddot{\mathbf{x}}_{r_{la}} - \dot{\mathbf{J}}_{v_{la}}(\mathbf{q})\dot{\mathbf{q}} \right) + \left(\mathbf{I} - \mathbf{J}_{v_{la}}(\mathbf{q})^+\mathbf{J}_{v_{la}}(\mathbf{q}) \right) \boldsymbol{\xi}, \qquad (24)$$

where

$$\ddot{\mathbf{x}}_{r_{la}} = \ddot{\mathbf{x}}''_{d_{la}} + \widehat{\ddot{\mathbf{x}}}_{h_{la}} - \mathbf{M}^{-1}_{v_d} \left(\mathbf{R}_{la}\ \mathbf{f}^e_{h_{la}} - \mathbf{B}_{v_d}\dot{\mathbf{e}}_{la} - \mathbf{K}_{v_d}\mathbf{e}_{la} \right),$$

$$\widehat{\mathbf{x}}_{h_{la}} = \mathbf{x}_{la} - \left(\widehat{\mathbf{K}}_{s_{la}} \right)^{-1} \mathbf{R}_{la}\ \mathbf{f}^e_{h_{la}},$$

$$\boldsymbol{\xi} = \mathbf{M}^{-1}_{\xi_{ua}}(\boldsymbol{\tau}_{\xi_{ua}} - \mathbf{B}_{\xi_{ua}}\dot{\mathbf{q}}),$$

$$\boldsymbol{\tau}_{\xi_{ua}} = \mathbf{J}^e_{v_{ua}}(\mathbf{q})^T\mathbf{K}_f \left(\mathbf{f}^e_{h_{d_{ua}}} - \mathbf{f}^e_{h_{ua}} \right),$$

$$\mathbf{e}_{la} = \mathbf{x}_{d_{la}} - \mathbf{x}_{la}, \quad \mathbf{x}_{d_{la}} = \mathbf{x}''_{d_{la}} + \widehat{\mathbf{x}}_{h_{la}}.$$

The reference position $\boldsymbol{q}_r$ for the joint-space position controller $C(s)$ in (18) is then obtained from (24) as $\boldsymbol{q}_r = \iint \ddot{\boldsymbol{q}}_r$. The reference-current-control-input $\boldsymbol{i}_r$ for n-CCDC-drives, generated by the DOB-based-DLTC then follows from (14), (15) and (16) as

$$\mathbf{i}_r = \mathbf{N}_{Dc_f}(s)\boldsymbol{\eta}^{-1}\boldsymbol{\tau}_L + \mathbf{H}_c\mathbf{K}^{-1}_{t_n}\boldsymbol{\tau}^*_e, \qquad (25)$$

where

$$\boldsymbol{\tau}^*_e = (\mathbf{I} - \mathbf{Q}_o(s))^{-1}\left(\boldsymbol{\tau}_r - \mathbf{Q}_o(s)\mathbf{G}^{-1}_{T_n}(s)\boldsymbol{\eta}\dot{\mathbf{q}}\right),$$

$$\boldsymbol{\tau}_r = \mathbf{C}(s)\boldsymbol{\eta}(\mathbf{q}_r - \mathbf{q}).$$

Here $\mathbf{H}_c = diag\{h_{c_j}\}$ is the current feedback gain matrix while $\mathbf{K}_{t_n} = diag\{k_{t_j}\}$ is the constant torque matrix for the CCDC-drives of the exoskeleton with j=1 to 4.

5. Simulation

A dynamic simulation model of the human-arm-exoskeleton system is first developed in Simulink^TM to validate its performance. The forward-dynamics of the exoskeleton are modelled using (2) while the forward-kinematics of the exoskeleton ($\mathbf{x}_{la}, \dot{\mathbf{x}}_{la}, \ddot{\mathbf{x}}_{la}, \mathbf{x}_{ua}, \dot{\mathbf{x}}_{ua}, \ddot{\mathbf{x}}_{ua},$) are modelled using transformations and equations defined in Appendix A. The actuators for the exoskeleton as CCDC-drives are modelled using Eqs. (10) and (11) whereas the compliant arm-supports of the exoskeleton are modelled as pure stiffness matrices $\mathbf{K}_{s_{ua}}$ and $\mathbf{K}_{s_{la}}$ using (19). A kinematic model of the human-arm is developed using the standard parameters of the human-arm for a 75 Kg man [41] w.r.t the base-frame $\sum_0$ of the exoskeleton. The human-arm kinematics is then used to find the human task-space positions $\mathbf{x}_{h_{la}}$ and $\mathbf{x}_{h_{ua}}$ for given human-arm joints angle $q_{h_1}, q_{h_2}, q_{h_3}$ and q_{h_4} while the interactive forces $\mathbf{f}_{h_{la}}, \mathbf{f}_{h_{ua}}$ on the human-arm are, in turn, found using (20). The kinematics and dynamics of both the human-arm and the exoskeleton are then used to model the dynamics of the human-arm-exoskeleton system.

Ideally, with no assistance provided to the human-arm, exoskeleton should not offer any resistance to the human movement, i.e., it should be purely transparent to the human with zero interactive force at the contact points. It is therefore proposed that the pHRI performance be evaluated in terms of the level of transparency of the exoskeleton, i.e., in terms of the magnitude of undesired interactive forces at the arm-supports. The developed model of the human-arm-exoskeleton system is, therefore simulated for the proposed control strategy in Fig. 4 to
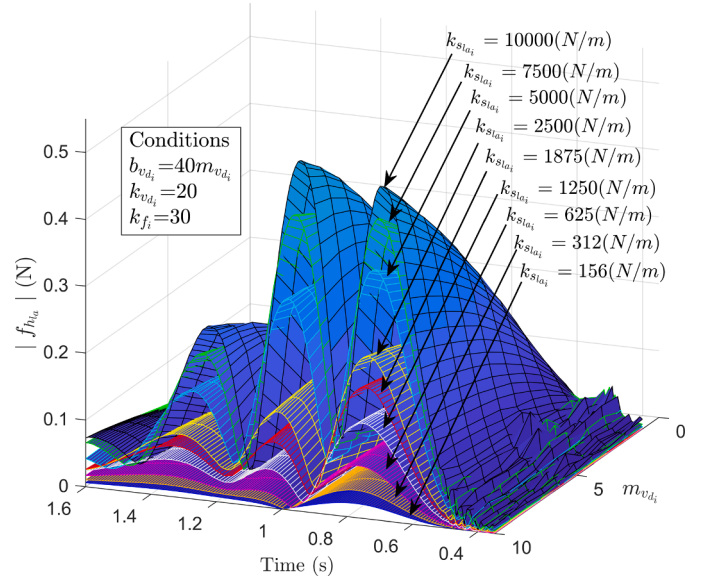

Fig. 7. Magnitude of human-interactive forces $|f_{h_{la}}|$ for different stiffness of compliant element $k_{s_{la}}$, plotted for increasing desired- impedance mass parameter $m_{v_{d_i}}$ (for i =1 to 3).

Fig. 8. Magnitude of human-interactive forces $|f_{h_{ua}}|$ for different stiffness of compliant element $k_{s_{ua}}$, plotted for increasing desired-impedance mass parameter $m_{v_{d_i}}$ (for i =1 to 3).

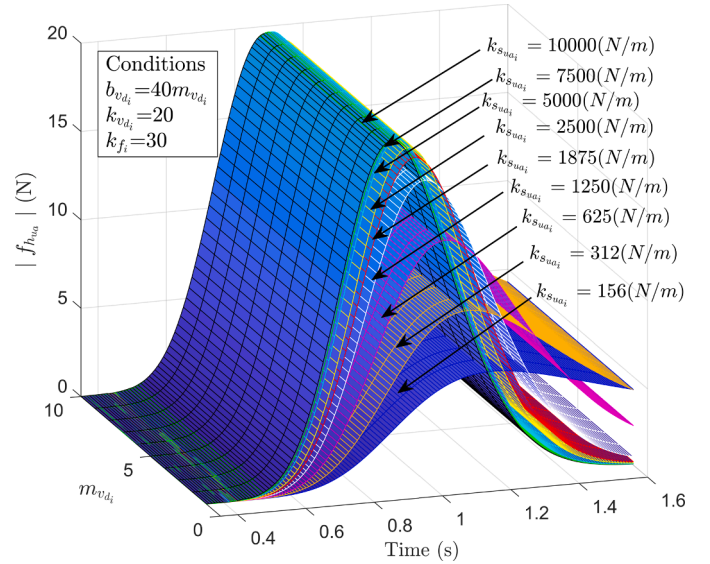analyze the amount of transparency afforded by the exoskeleton under zero human assistance condition (i.e., with external desired acceleration $\ddot{\mathbf{x}}'_{d_{la}}$=0). The transparency at the two arm-supports is analyzed w.r.t different stiffnesses of passive-compliant elements for different values of desired-impedance. That is for given support-stiffnesses $k_{s_{la_i}}$, $k_{s_{ua_i}}$ in (19) and desired-impedance values in (4), the pHRI performance is validated in terms of least interactive forces $\mathbf{f}_{h_{la}}, \mathbf{f}_{h_{ua}}$ at the respective arm-supports in the frame $\sum_o$. This analysis is performed by simulating the human-exoskeleton system for a 20° step-change in the human-arm joints angle $q_{h_1}, q_{h_2}, q_{h_3}$ and q_{h_4}. Furthermore, to affirm the pHRI performance for a worst-case scenario, the human-arm is presumed to be infinitely stiff, i.e., it is assumed that there is no effect on the task-space motion and position of the human-arm due to the interactive forces and all the effect is left to be mitigated by the exoskeleton alone.
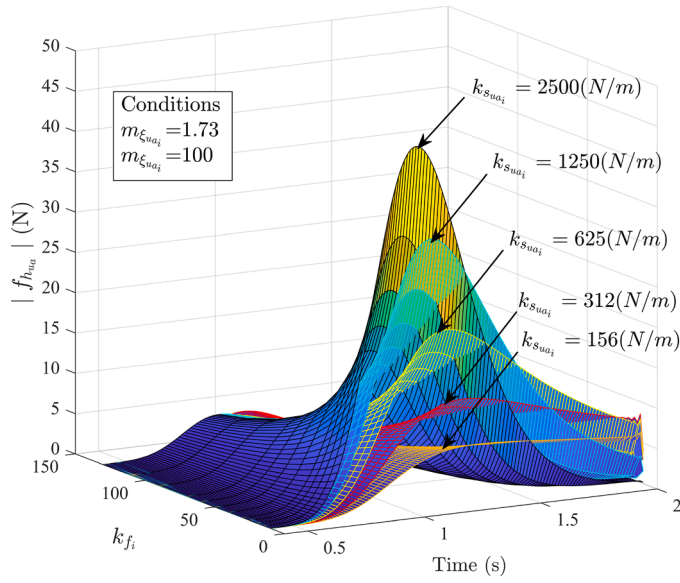
Fig. 9. Magnitude of human-interactive force $|f_{h_{ua}}|$ for different stiffness of compliant element $k_{s_{ua_i}}$, plotted for increasing force controller gain k_{f_i} (for $i = 1$ to 3).
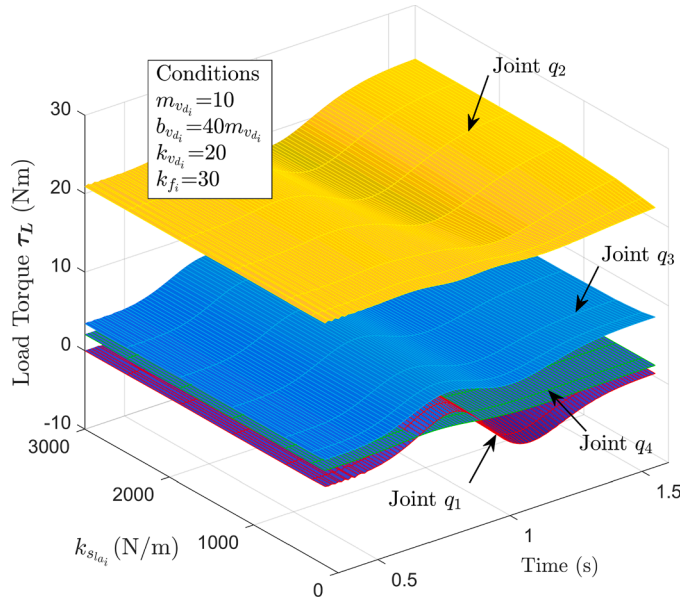

Fig. 10. Joint load-torques of 4-ADOF arm-exoskeleton, plotted for increasing support-stiffness k_{sla_i} (for $i = 1$ to 3).

The frequency content in the step change for the human joints is limited to 5 Hz, which is more than twice the maximum expected joint-frequency of humans for normal daily activities [42]. For the given desired acceleration $\ddot{x}_{d_{la}}$ (which is zero in our case), and estimated forces $\mathbf{f}_{h_{la}}$, $\mathbf{f}_{h_{ua}}$, the reference joint-space acceleration $\ddot{q}_r$ is found using the proposed control law in (24), whereas the reference-current-control-input $\mathbf{i}_r$ for CCDC-drive actuators is found using (25). The desired-impedance is varied by varying the mass parameter $m_{v_{d_i}}$ while keeping the damping parameter $b_{v_{d_i}}$ to be forty times $m_{v_{d_i}}$, to have an over damped error-response of the impedance control law in (4), so as to ensure stability.

The interactive force $|f_{h_{la}}|$ for increasing values of lower-arm support arm stiffness k_{sla_i} and desired-impedance values are shown in Fig. 7. It is noted that $|f_{h_{la}}|$ decreases with a decrease in both k_{sla_i} and $m_{v_{d_i}}$. It is
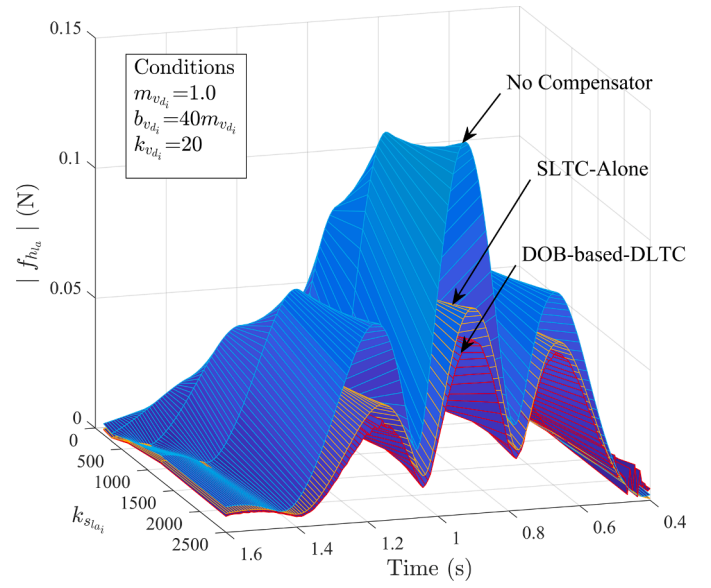

Fig. 11. Magnitude of human-interactive forces $|f_{h_{la}}|$ for different load-torque compensators, plotted for increasing support-stiffness k_{sla_i} (for $i = 1$ to 3).

observed that because of the finite dynamics of the limited-power-actuators along with the associated delay due to position control, the reference acceleration $\ddot{x}_{r_{la}}$ dictated by the impedance control law in (4) is not precisely tracked. Therefore, for a given desired-impedance, the passive stiffness of compliant elements at the lower-arm support is observed to have a significant effect in reducing the magnitude of the undesired interactive force $f_{h_{la}}$. This hence improves the transparency and, in turn, the pHRI performance of the exoskeleton at the lower-arm.

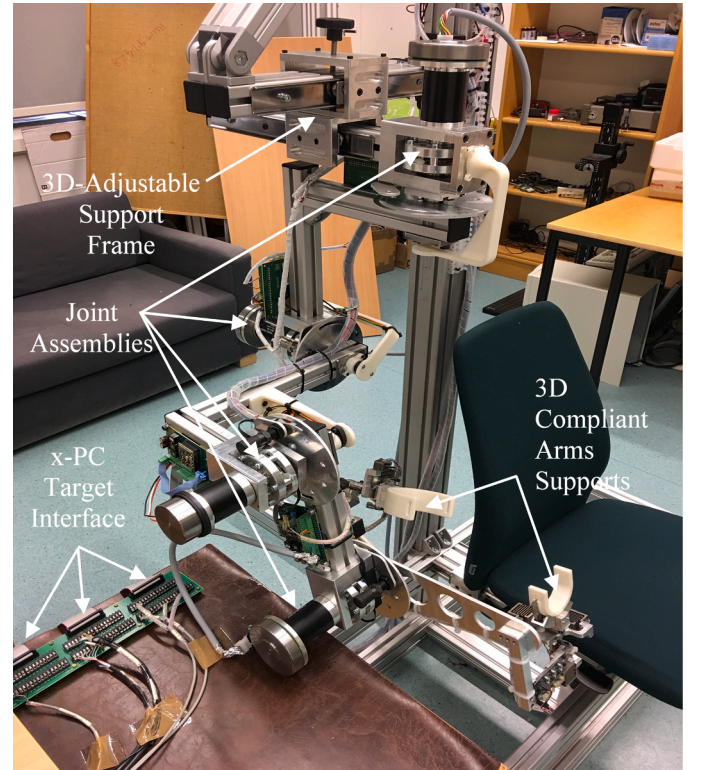The upper-arm support, on the other hand, is controlled in the null

Fig. 12. Realized 4-ADOF arm-exoskeleton test-rig with passive-compliant arm-support.
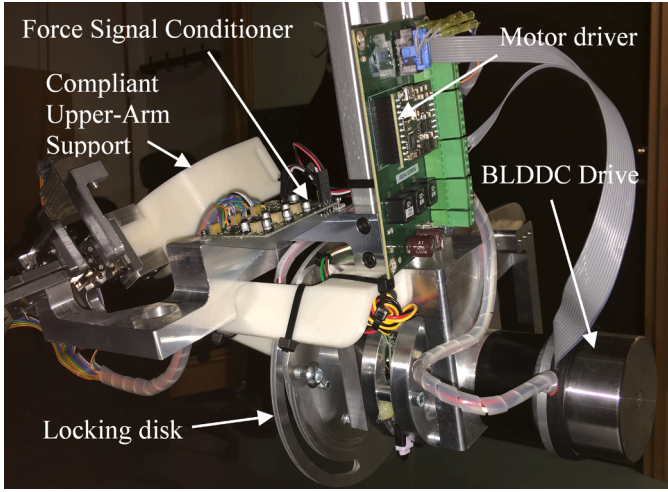
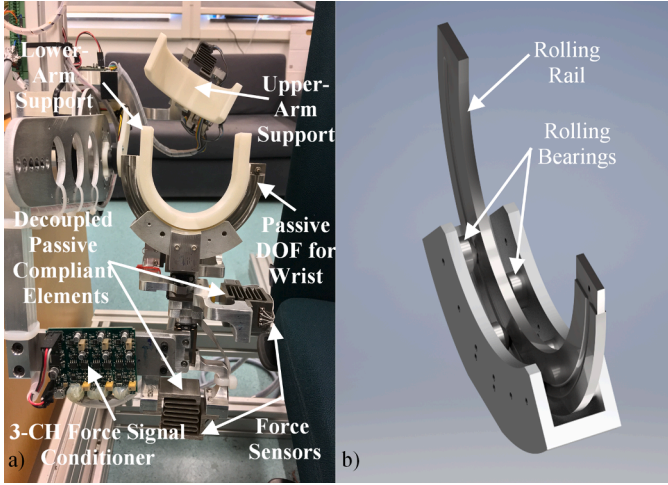**Fig. 13.** Close up view of the developed joint actuator-assembly.

Fig. 14. (a): Close up view of realized lower-arm support (b): Close-up view of mechanism for frictionless passive wrist movement.

space of the lower-arm support Jacobian $J_{v_{la}}(q)$. The effect on $|f_{h_{ua}}|$ for increasing value of $k_{s_{ua_i}}$ and $m_{v_{d_i}}$ is shown in Fig. 8 and it is observed that for a given force controller gain K_f, the interactive force $|f_{h_{ua}}|$ at the upper-arm is not effected by the desired-impedance values. The support-stiffness $k_{s_{ua_i}}$ at the upper-arm therefore has a much stronger effect on $|\mathbf{f}_{h_{ua}}|$ and hence on the pHRI performance of the exoskeleton. The relatively large interactive forces at the upper-arm support shown in Fig. 8 can be significantly reduced by proper selection of the force controller gain k_{f_i}. The effect of k_{f_i} on $|f_{h_{ua}}|$ for different values of $k_{s_{ua_i}}$ is shown in Fig. 9. It is therefore seen from Fig. 9 that for a given value of k_{f_i}, lower values of support-stiffness $k_{s_{ua_i}}$ can significantly reduce the undesirable interactive forces at the upper-arm support and can hence meaningfully improve the transparency and, in turn, the pHRI performance of the exoskeleton.

The load-torques for the four joints of the exoskeleton are plotted in Fig. 10 vs $k_{s_{la_i}}$ for the proposed control strategy in Fig. 4 to not only validate the choice of selected joint actuators but also to ascertain the amount of variation in the joint load-torques due to variation is stiffness $k_{s_{la_i}}$. It is seen from Fig. 10 that the load-torques for all the joints are sufficiently less than the rated torques for the selected actuators shown in Table C4 in Appendix C, over a range of support-stiffness values. Therefore, the results in Fig. 10 validate the choice of selected joint

actuators for proper empirical testing of the proposed control strategy, over a range of support-stiffness values.

To compare the task-space performance of the proposed load-torque compensator (DOB-based-DLTC) for the control strategy in Fig. 4, the modelled human-exoskeleton system is also simulated for different load-torque compensators over a range of stiffness values. The performance of these load-torque compensators for a single joint has been discussed in detail in [34]. The interactive force $|\mathbf{f}_{h_{la}}|$ for different load-torque compensators, plotted for increasing support-stiffness $k_{s_{la_i}}$ is shown in Fig. 11. The comparative results in Fig. 11 are obtained for a low desired-impedance value without saturating the joint-actuators. It is seen from Fig. 11 that the modelled human-exoskeleton system using the proposed DOB-based-DLTC gives the least undesired interactive force $|\mathbf{f}_{h_{la}}|$ as compared to when simulated with standard Static Load-Torque Compensator (SLTC) or No-Compensator over a range of support-stiffness values. Thus, the proposed compensator outperforms the other compensators in improving the transparency and hence ensures an improved pHRI performance for the exoskeleton.

6. 4-ADOF arm-exoskeleton test-RIG

In order to practically verify the proposed strategy for improved pHRI performance, a specific arm-exoskeleton test-rig is developed, as shown in Fig. 12. This rig broadly compromises of a 4-ADOF exoskeleton with an adjustable support base. Unique four actuator-assemblies were designed for each joint of the proposed exoskeleton with integrated torques-sensors, absolute/incremental encoders, CCDC-drives, locking disks, and torque-signal conditioners. A close-up view of one such assembly is shown in Fig. 13. Specifications of the selected actuators are listed in Appendix C, along with the allowed range of motion for each joint as per DH-convention. To ensure accurate sensing of the axial joint load-torques by the torque sensors, the joint assemblies are specially designed so that all the radial structural-loads on the joint shafts are transmitted to the respective joint assemblies and not to the coupled load-torque sensors. This approach in-turn protects the joint torque sensor from sensing unwanted radial torques arising due to the structural load of the exoskeleton. Two novel mechanically-decoupled 3-D compliant arm-supports with integrated force-sensors are also designed for the exoskeleton, as shown in Fig. 14 (a). To ensure decoupled force sensing, the interactive-force component along a particular spatial axis (in the local-frame $\sum_{ua}$ or $\sum_{la}$) is independently sensed by the respective force sensor on the individual compliant element. A passive degree of freedom using miniature roller bearings is provided for the wrist movement at the lower-arm support to provide comfort to the user, as shown in Fig. 14 (b).

Real-time hardware in the loop testing of the developed exoskeleton test-rig is performed using Simulink xPC-Target^{TM} setup, using two dedicated computers. All the sensors and actuators of the test-rig are interfaced to an xPC-Target computer using Humusoft^{TM} I/O cards. The xPC-Host computer is linked to the xPC-Target computer through a dedicated Ethernet connection for not only downloading the generated real-time code but also is used to control and configure the xPC-Target computer. The proposed control strategy is compiled on the Host-PC and then download to the Target-PC to be implemented in real-time on the exoskeleton. The real-time results are then obtained on the Host-PC via the same dedicated Ethernet link.

7. Experimental results

To experimentally validate the pHRI performance afforded by the proposed control strategy, it is proposed that the exoskeleton should be practically analyzed for transparency with no assistance offered to the human, as discussed in detail in Section 5. That is a desired-trajectory be generated by an external system coupled to the exoskeleton, and the exoskeleton tries to follow the desired-trajectory with the least possible
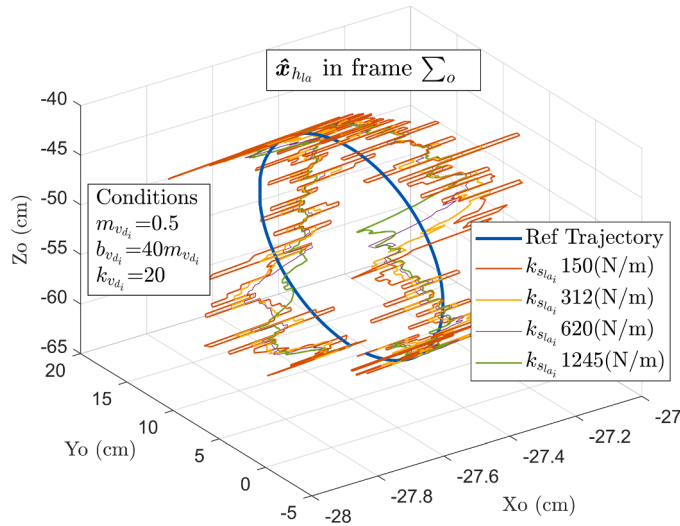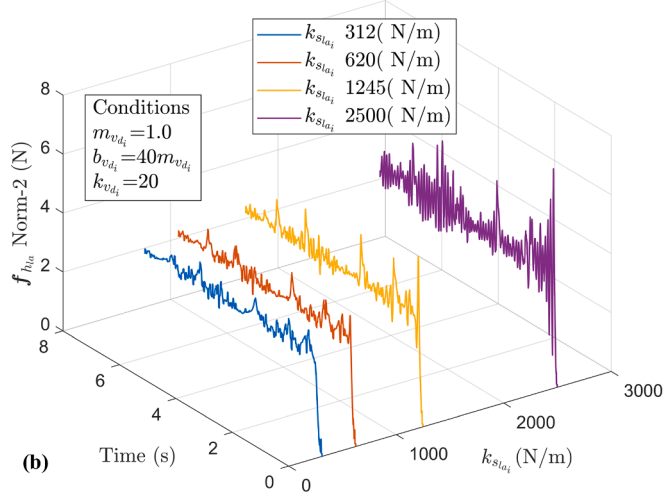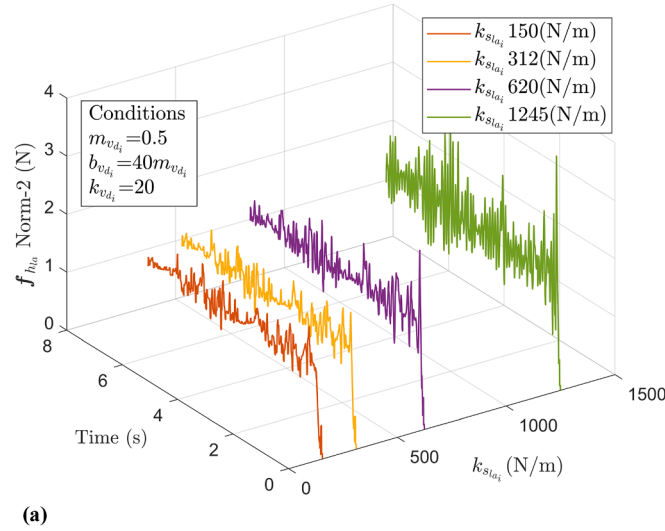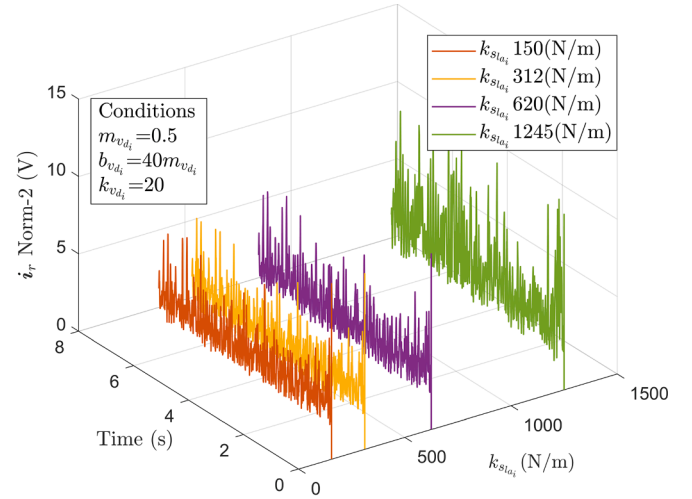
Fig. 15. Reference trajectory and estimated human-arm task-space position $\widehat{x}_{h_{la}}$ at the lower-arm support.

interactive-forces at the point of contact. For the analysis to be scientifically viable, it is required that all other variables affecting the interactive-forces (i.e., contact-point impedance of the externally coupled system, path, and speed of the desired trajectory) should be kept constant except for the stiffness of the compliant elements for which the proposed strategy is being analyzed. The actual human-arm cannot be used as an externally-coupled system to practically validate the proposed strategy because the human-arm not only tends to offer a variable contact-point impedance [43,44] while moving in task-space, but it is also hard for the human-arm to persistently generate the same desired trajectory, with the same speed for different passive-compliant elements in question. An industrial robotic-arm, on the other hand, not only offers a constant contact-point impedance, but it can also persistently generate the desired trajectory with the same speed for each trial of the experiment. Furthermore, it is well-known that the stability of the contact-point coupled-systems (exoskeleton-human or exoskeleton-robot) is the least when the impedance of one of the coupled-systems is a maximum [45,46]. Therefore, in order to verify the proposed strategy for the worst-case scenario (infinitely stiff human-arm) as discussed in Section 5, it is required that the external-system coupled to the exoskeleton offers a maximum contact point impedance, i.e., it is infinitely rigid w.r.t exoskeleton.
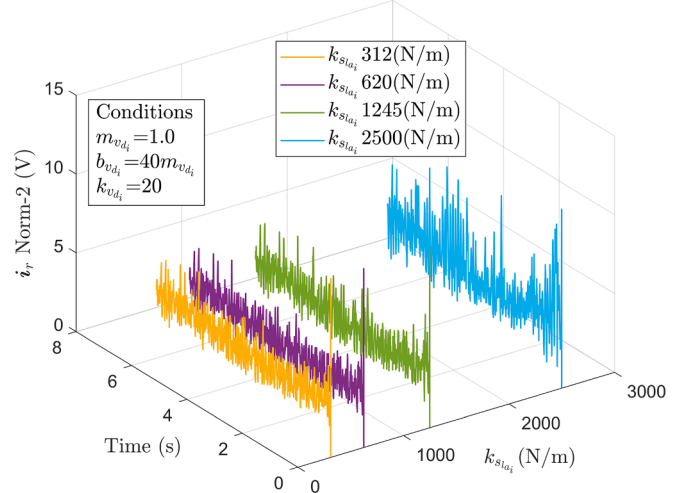

Fig. 16. Experimental comparative results for the proposed control strategy in Fig. 4 for different values of compliant element stiffness $k_{s_{lai}}$ for an infinitely stiff human-arm. (a): Magnitude of human-interactive forces $|\mathbf{f}_{h_{la}}|$ at lower-arm support for $m_{v_{d_i}}$=0.5 (b): Magnitude of human-interactive forces $|\mathbf{f}_{h_{la}}|$ at lower-arm support for $m_{v_{d_i}}$=1.0. (c): Magnitude of reference-current-control-input $|\mathbf{i}_r|$ for the joint actuators with $m_{v_{d_i}}$=0.5. (d): Magnitude of reference-current-control-input $|\mathbf{i}_r|$ for the joint actuators with $m_{v_{d_i}}$=1.0.

Table 2
Improvement in pHRI in terms of $|f_{h_{la}}|_{dB}$ and $|f_{h_{la}}|_{jitter_{dB}}$.

$m_{v_{d_i}}$	$k_{s_{la_i}}$ (N/m)	$|f_{h_{la}}|_{dB}$	$|f_{h_{la}}|_{jitter_{dB}}$
1.0	620	-0.60 dB	-0.63 dB
	312	-1.89 dB	-1.81 dB
0.5	620	-1.14 dB	0.90 dB
	312	-2.22 dB	-1.95 dB
	150	-4.18 dB	-3.90 dB

For these reasons, a 7-DOF KUKA industrial robotic-arm was used as an external system, coupled at the lower-arm support to experimentally verify the transparency of the exoskeleton and hence the pHRI performance for the worst-case scenario. The robotic-arm is programmed to accurately track a reference task-space trajectory of 10 cm radius at 1 rad/s in the X-Z plane of the base-frame $\sum_0$. The reference trajectory for the KUKA robot is shown in Fig. 15. The exoskeleton is then made to follow the KUKA-robot's end-effector position at the lower-arm support by using the proposed control strategy shown in Fig. 4. The designed xPC-Target interface is used to impart real-time control to the 4-ADOF exoskeleton. The experiment is repeated for increasing stiffness of passive- compliant elements $k_{s_{la_i}}$ and the desired contact-point impedance of the exoskeleton.

Correct practical implementation of the proposed control strategy in

Fig. 4 requires a reasonably accurate estimate of the human-arm task-space position $\widehat{x}_{h_{la}}$ at the lower-arm support. The human-arm position (position of KUKA-robot end-effector in our case) at the lower-arm support can be estimated by using the stiffness estimate $\widehat{K}_{s_{la}}$ of lower-arm support as, suggested in (22). Since the stiffness of the lower-arm support is significantly reduced by the use of passive-compliant elements, the error in the estimation of $\widehat{K}_{s_{la}}$ is naturally reduced. Therefore, a reasonably accurate estimate of human-position is now possible without the use of additional sensors. The estimated human arm task-space position $\widehat{x}_{h_{la}}$ is plotted in Fig. 15 in comparison with the reference trajectory for different values of compliant element stiffness $k_{s_{la_i}}$ and it is seen that $\widehat{x}_{h_{la}}$ is estimated fairly accurately using the suggested approach.

The measured interactive force $|f_{h_{la}}|$ at the lower-arm support for increasing value of $k_{s_{la_i}}$ for an infinitely stiff human-arm is shown in Fig. 16. The results are obtained for two different values of the desired-impedances and are respectively shown in Fig. 16 (a) and (b). The selected desired- impedances are primarily defined by the mass parameter $m_{v_{d_i}}$ as discussed in detail in Section 5. It is seen that not only the magnitude of undesired interactive forces decreases with the decrease in stiffness $k_{s_{la_i}}$ of the passive-compliant elements but the noise jitter in $\mathbf{f}_{h_{la}}$ also reduces for both the desired-impedance values. This, in
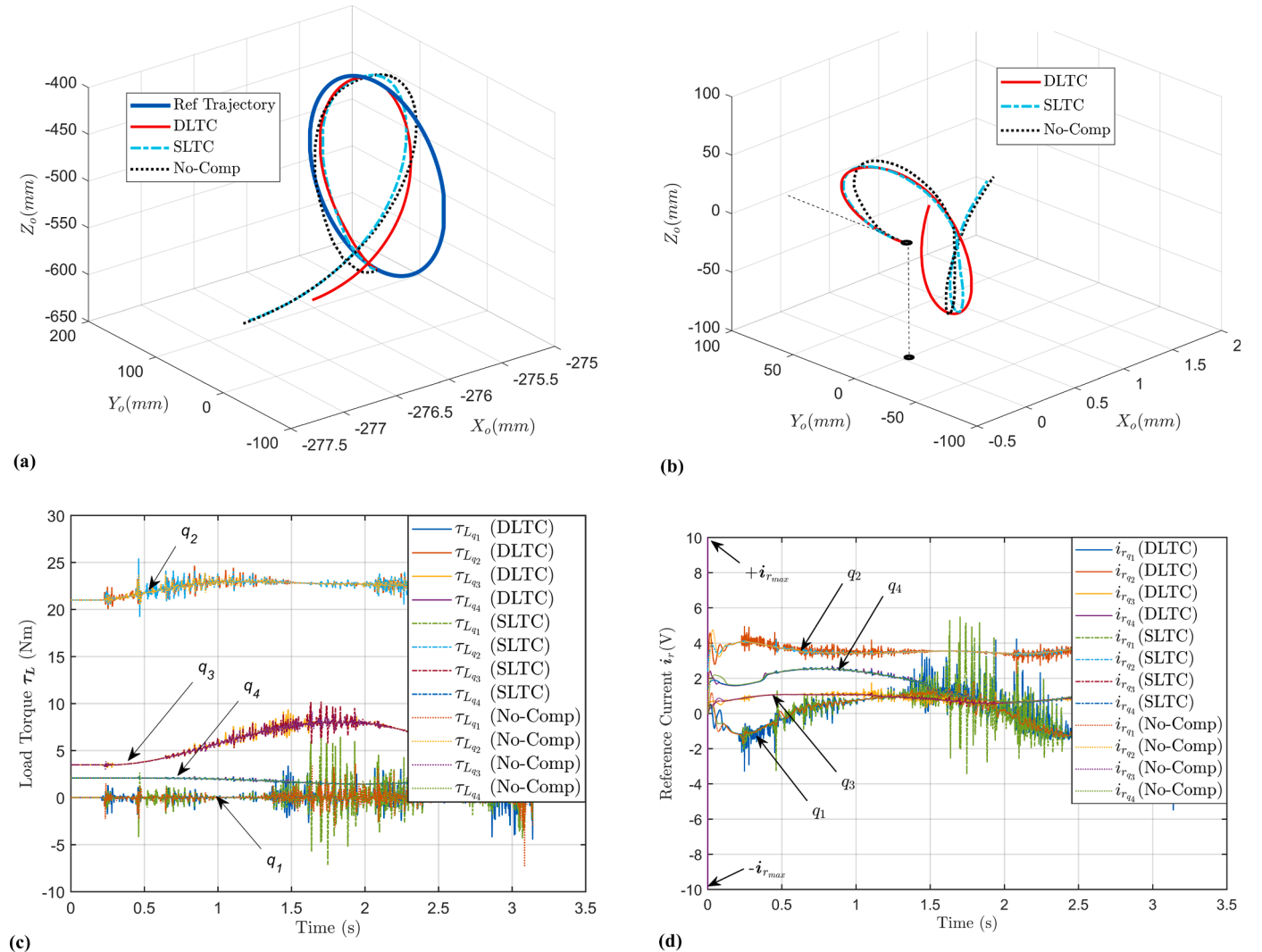

Fig. 17. Experimental comparative results for open-loop task-space position tracking at lower-arm support for different load-torque compensators. (a): 3-D circular trajectory tracking. (b): 3-D tracking-error. (c): Measured joint load-torques τ_L. (d): Reference-current-control-input i_r.

12

turn, naturally improves the stability as well as the fidelity of the impedance control at the lower-arm support. Furthermore, it is seen that for the same values of support-stiffness $k_{s_{la_i}}$., the magnitude of human-interactive forces is lower for lower desired-impedance, which is in accordance with the simulation results shown in Fig.7 in Section 5. The empirical improvement in pHRI performance w.r.t decrease in arm-support-stiffness $k_{s_{la_i}}$ is quantified in Table 2. in terms of attenuations $|\mathbf{f}_{h_{la}}|_{dB}$ and $|\mathbf{f}_{h_{la}}|_{jitter_{dB}}$. for the two desired- impedance values. The attenuations $|\mathbf{f}_{h_{la}}|_{dB}$ and $|\mathbf{f}_{h_{la}}|_{jitter_{dB}}$ are defined in the digital mean square sense as

$$|\mathbf{f}_{h_{la}}|_{dB} = 20 log_{10}\left(\sqrt{\frac{\sum |\mathbf{f}_{h_{la}}|^2}{\sum |\mathbf{f}_{h_{la}}|_{ref}^2}} \right),$$

$$|\mathbf{f}_{h_{la}}|_{jitter_{dB}} = 20 log_{10}\left(\sqrt{\frac{\sum |\mathbf{f}_{h_{la}}|_{jitter}^2}{\sum |\mathbf{f}_{h_{la}}|_{jitter_{ref}}^2}} \right).$$

Where $|\mathbf{f}_{h_{la}}|_{jitter}$ is the jitter in $|\mathbf{f}_{h_{la}}|$ while $|\mathbf{f}_{h_{la}}|_{ref}$ and $|\mathbf{f}_{h_{la}}|_{jitter_{ref}}$ are the respective references for force and jitter, found for a support-stiffness of 1245 N/m. It is, therefore, seen quantitatively from Table. 2 that the pHRI performance of the exoskeleton is improved by the decrease in the passive-stiffness of the arm-supports in terms of reduction in both the interactive forces as well as the noise-jitter. It is also noted that the improvement in pHRI performance is more for the lower value of desired-impedance with $m_{v_{d_i}} = 0.5$. This is in accordance with the simulation results in Fig. 7 as the tracking errors are larger for lower values of desired-impedance (as discussed in detail Section 5), and hence, lower values of passive-support-stiffness have a larger role to play in reducing the undesired interactive forces.

The magnitude of measured reference-current-control-input $|i_r|$ for the exoskeleton's joint-actuators in volts is shown in Fig. 16. These results are also obtained for two different values of desired-impedances and are respectively shown in Fig. 16 (c) and (d). It is noted that the reference-current-control-input requirement for the joint actuators also decreases with a decrease in $k_{s_{la_i}}$ for both the desired-impedance values. It was observed that for the given experiment it was not possible to realize the desired-impedance with $m_{v_{d_i}} = 0.5$ for $k_{s_{la_i}}$ values greater than 1245 (N/m), without saturating the joint-actuators of the exoskeleton (i. e., $|i_r| > 10V$). Similarly, for the desired-impedance with $m_{v_{d_i}} = 1$, the limiting value of $k_{s_{la_i}}$ was found to be 2500 N(/m). Therefore, it is empirically seen that decreasing the stiffness of the arm supports makes the actuators of the exoskeleton less prone to saturation and in turn, enables lower values of desired-impedance to be effectively realized for limited power actuators, without compromising the stability of the system. Lower realizable values of impedance imply better transparency of the exoskeleton and hence, in turn, an improved pHRI performance of the exoskeleton. The lower limit for $k_{s_{la_i}}$ on the other hand, is found to be primarily limited by the amount of mechanical displacement allowed for each compliant element. For the desired-impedances with $m_{v_{d_i}} = 0.5$ and $m_{v_{d_i}} = 1$, the respective lower limits for $k_{s_{la_i}}$ were found to be 150 (N/m) and 312 (N/m) for a permissible mechanical displacement of 10 mm.

In order to explicitly see the practical improvement afforded by the proposed DOB-based-DLTC, the test-rig is also operated under open-loop position control in 3-D task-space (w.r.t frame $\sum_o$), to track a 10-cm radius circular reference trajectory, at 0.32 Hz at the lower-arm support. The relative position tracking performance for different load torque compensators is shown in Fig. 17(a) and (b). The measured joint load-torques produced during tracking for different compensators are shown in Fig. 17 (c) while the generated reference-current-control-inputs for each joint actuator are shown in Fig. 17 (d). It is seen from Fig. 17 (a) and (b) that the proposed compensator achieves an improved tracking performance with lower and steady task-space error as
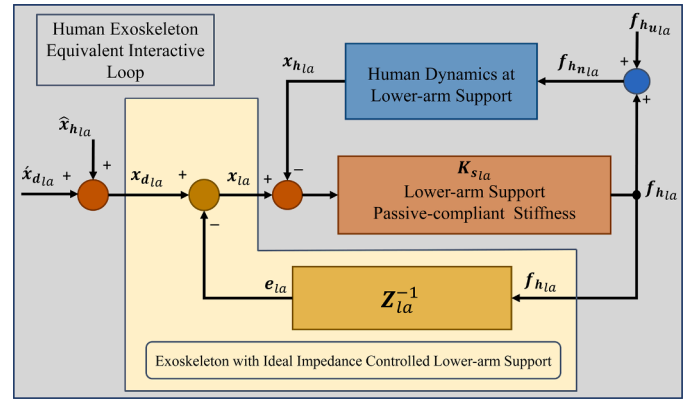

Fig. 18. Human-exoskeleton equivalent interactive loop for ideal impedance controlled lower-arm support with passive compliance.

compared to SLTC and No-Compensator. It is also seen from Fig. 17 (d) that the improved performance is achieved with comparable reference-current requirements without saturating the joint actuators. Better tracking ensures better realization of desired-impedance and hence lower interactive forces, which in turn, improve the transparency and, therefore, the pHRI performance of the exoskeleton.

In the actual scenario, when a real human subject is used the interactive forces at the human-arm might be different from the forces shown in Fig. 6 for the same desired trajectory, but the interactive forces would always be less than the worst-case scenario implemented here because the contact impedance of the human is always very less than that of the industrial robotic-arm. Therefore, the proposed control strategy, along with the passive-compliant arm-support, is expected to provide better and safer-pHRI performance for the actual human subject.

8. Significance

To mathematically see the significance of using passive-compliant supports for safe-pHRI, it is assumed that the lower-arm support is under ideal impedance control with infinite bandwidth actuators. The $\ddot{x}_{la}$ then accurately tracks $\ddot{x}_{r_{la}}$ dictated by the impedance control law in (4). The exoskeleton impedance at the lower-arm is therefore equal to the desired-impedance which can be given in terms of $\mathbf{f}_{h_{la}}$ and $\mathbf{e}_{la}$ in Laplace-domain from (3), (20) and Appendix B as $\mathbf{Z}_{d_{la}}(s)\mathbf{e}_{la}(s) = \mathbf{f}_{h_{la}}(s)$. Here $\mathbf{Z}_{d_{la}}(s)$ is the complex ideal impedance matrix of the lower-arm support given by $\mathbf{Z}_{d_{la}}(s) = \mathbf{M}_{v_d}s^2 + \mathbf{B}_{v_d}s + \mathbf{K}_{v_d}$. If the lower-arm support is considered to be under practical impedance control with limited bandwidth actuators, then the complex actual-impedance $\mathbf{Z}_{la}(s)$ at the lower-arm can similarly be given in terms of $\mathbf{f}_{h_{la}}$ and $\mathbf{e}_{la}$ as

$$\mathbf{Z}_{la}(s)\mathbf{e}_{la}(s) = \mathbf{f}_{h_{la}}(s), \tag{26}$$

where

$$\mathbf{f}_{h_{la}}(s) = \mathbf{K}_{s_{la}}\left(\mathbf{x}_{la}(s) - \mathbf{x}_{h_{la}}(s)\right),$$

$$\mathbf{Z}_{la}(s) = \mathbf{M}_{v_{la}}s^2 + \mathbf{B}_{v_{la}}s + \mathbf{K}_{v_{la}},$$

$$\mathbf{M}_{v_{la}} = \mathbf{M}_{v_d} + \mathbf{\Delta M}_v,$$

$$\mathbf{B}_{v_{la}} = \mathbf{B}_{v_d} + \mathbf{\Delta B}_v,$$

$$\mathbf{K}_{v_{la}} = \mathbf{K}_{v_d} + \mathbf{\Delta K}_v.$$

Here $\mathbf{\Delta M}_v$, $\mathbf{\Delta B}_v$ and $\mathbf{\Delta K}_v \in \mathbb{R}^{3 \times 3}$ respectively represent the deviation in mass, damping, and stiffness matrices from the desired ones in Appendix B. This deviation then implies that the actual impedance $\mathbf{Z}_{la}$ of the exoskeleton at the lower-arm would deviate from the desired-impedance

$Z_{d_{la}}$ due to the limited bandwidth of the joint actuators. Under ideal impedance control assumption $\Delta \boldsymbol{M}_v$, $\Delta \boldsymbol{B}_v$ and $\Delta \boldsymbol{K}_v$ are null matrices and $\boldsymbol{Z}_{la} = \boldsymbol{Z}_{d_{la}}$.

The equivalent human-exoskeleton interactive loop for the impedance controlled lower-arm support (with passive compliance) along with the coupled human-arm dynamics is shown in Fig. 18. If $\mathbf{f}_{h_{la}}$ is the task-space force applied on the human-arm by the exoskeleton and $\mathbf{f}_{h_{u_{la}}}$ is the voluntary force applied by the human himself at the lower-arm contact then the net task-space force applied on the human-arm at the lower-arm contact is $\mathbf{f}_{h_{n_{la}}} = \mathbf{f}_{h_{u_{la}}} + \mathbf{f}_{h_{la}}$. The position $\boldsymbol{x}_{la}$ can be written from (3) as $\mathbf{x}_{la} = \mathbf{x}_{d_{la}} - \mathbf{e}_{la}$, therefore, $\mathbf{f}_{h_{la}}$ can be written in Laplace-domain from in (20), (21) and (26) as

$$\mathbf{f}_{h_{la}}(s) = \mathbf{P}_{la}^{-1}(s)\mathbf{K}_{s_{la}}\mathbf{x}^{''}{}_{d_{la}}(s) + \mathbf{P}_{la}^{-1}(s)\mathbf{K}_{s_{la}}\left(\widehat{\mathbf{x}}_{h_{la}}(s) - \mathbf{x}_{h_{la}}(s)\right), \tag{27}$$

where $\boldsymbol{P}_{la}(s) = (\mathbf{I} + \mathbf{K}_{s_{la}}\mathbf{Z}_{la}^{-1}(s))$. If the deviation matrices $\Delta \boldsymbol{M}_v$, $\Delta \boldsymbol{B}_v$ and $\Delta \boldsymbol{K}_v$ in (26) are considered diagonal then $\boldsymbol{Z}_{la}(s)$ and hence the matrix $\boldsymbol{P}_{la}(s) \in \mathbb{R}^{3 \times 3}$ in (27) is also diagonal i.e. $\boldsymbol{Z}_{la}(s) = diag\{z_{la}(s)_i\}$, $\boldsymbol{P}_{la}(s) = diag\{p_{la}(s)_i\}$. The diagonal elements of $\boldsymbol{Z}_{la}(s)$ and $\boldsymbol{P}_{la}(s)$ are hence given by

$$z_{la}(s)_i = \left(m_{v_{d_i}} + \Delta m_{v_i}\right)s^2 + \left(b_{v_{d_i}} + \Delta b_{v_i}\right)s + \left(k_{v_{d_i}} + \Delta k_{v_i}\right), \tag{28}$$

where $i = 1$ to 3. Therefore, the task-space interactive-force components $f_{h_{la_i}}$ for lower-arm support can be written independently from (19), (27) and (28) as

$$f_{h_{la_i}}(s) = z_{app_{la}}(s)_i x^{'}{}_{d_{la}}(s)_i + z_{app_{la}}(s)_i\left(\widehat{x}_{h_{la}}(s)_i - x_{h_{la}}(s)_i\right), \tag{29}$$

where

$$z_{app_{la}}(s)_i = \frac{z_{la}(s)_i\, k_{s_{la_i}}}{z_{la}(s)_i + k_{s_{la_i}}}, \quad i = 1 \text{ to } 3.$$

It is seen from (29) that w.r.t the modified desired input $x^{'}{}_{d_{la_i}}$, for any frequency, the respective apparent impedance of lower-arm support $z_{app_{la}}(s)_i$ along the ith task-space axis is a parallel combination of the corresponding actively controlled impedance $z_{la}(s)_i$ and the stiffness of the respective passive-compliant element $k_{s_{la_i}}$. Therefore, no matter how far the actual impedance $z_{la}(s)_i$ is from the desired value, due to bandwidth or saturation limitation of the actuators, the apparent impedance $z_{app_{la}}(s)_i$ would always be limited by the stiffness of the passive-compliant element $k_{s_{la_i}}$ along the ith task-space axis. Thus, the inclusion of mechanically decoupled passive-compliant elements in the arm-support ensures a safe-pHRI by limiting the amount of maximum impedance experienced by the human. Furthermore, it is seen from (29) that the corresponding apparent impedance $z_{app_{la}}(s)_i$ w.r.t modified input $x^{'}{}_{d_{la_i}}$ also acts as a gain for the error in the estimation of the human-arm position at lower-arm contact. Therefore, a lower stiffness value of passive-element $k_{s_{la_i}}$ is suggested to limit the apparent impedance to a lower value. However, on the other hand, the value of $k_{s_{la_i}}$ cannot be very low as this would limit the maximum control range of the desired-impedance for the lower-arm support. A very low desired-impedance, as clear from (4) and (7), will dictate large task-space accelerations and, in turn, large joint-space accelerations, which are difficult to track

with limited power actuators, having limited bandwidth. Thus, the desired low impedance would not be tracked, and the apparent impedance response would primarily be passive and uncontrolled, dictated by the stiffness $k_{s_{la_i}}$ of the passive elements alone at the lower-arm support. It is therefore, suggested that a suitable stiffness value of $k_{s_{la_i}}$ is chosen (while considering the power and bandwidth limitation of the actuators) to allow a sufficient range of desired-impedance, for proper implementation of the impedance control in (4) and, in turn, the control strategy in Fig. 4.

9. Conclusion

For a 4-ADOF exoskeleton as a LADOF assistive device, it is shown in this paper through simulation and experimentation that by using a position-based impedance control law (for increased stability) and using limited power and bandwidth joints actuator (for lower weight) the price paid in terms of increased human-interactive-forces at the arm-supports can adequately be compensated by using the proposed mechanically decoupled compliant arm-supports with lower stiffness values. It is further shown both through simulation and experimentation that the suggested novel DOB-based-DLTC in vectoral-form can more efficiently linearize and decouple the human-exoskeleton system as compared to the classical SLTC by providing a more effective load-torque compensation for all the n active joints of the exoskeleton. It is therefore concluded that if active impedance control is used in combination with decoupled passive-compliant end-supports, as suggested, with an effective joint load-torque compensation scheme, as suggested, an improved and safer pHRI performance in terms of low human-interactive forces can be achieved. Furthermore, it is shown that improvement in pHRI achieved by using the suggested two-arm support approach with 3-D force-sensing only requires a computationally efficient linear task-space reference acceleration ($\ddot{\mathbf{x}}_{r_{v_{la}}}$) values for its implementation without requiring to compute the intricate angular acceleration part ($\ddot{\mathbf{x}}_{r_{\omega_{la}}}$). It is also mathematically shown that the maximum task-space impedance experienced by the human is always limited by the stiffness of the individual compliant element at the lower arm-support, which in turn, ensures a safer-pHRI.

CRediT authorship contribution statement

Declaration of Competing Interest

The authors declare that they have no known competing financial interests or personal relationships that could have appeared to influence the work reported in this paper.

Acknowledgment

A. Appendix

Transformation matrices for arm-supports

The current task-space positions $\boldsymbol{x}_{la}$, $\boldsymbol{x}_{ua} \in \mathbb{R}^3$ and the orientation matrices $\boldsymbol{R}_{ua}$, $\boldsymbol{R}_{la}$ of the upper and lower-arm supports for the current joint position, $\boldsymbol{q}$ are given by the respective homogeneous transformation matrices $\boldsymbol{T}_{ua}(\boldsymbol{q})$, $\boldsymbol{T}_{la}(\boldsymbol{q}) \in \mathbb{R}^{4 \times 4}$ [47], and are defined as

Table A1
D-H parameters for the 4-ADOF arm exoskeleton*

$a_i(m)$	$d_i(m)$	$\alpha_i(rads)$	$q_{i0}(rads)$
$a_1 = 0$	$d_1 = -0.414$	$\alpha_1 = \pi/2$	$q_{0_1} = \pi/2$
$a_2 = 0$	$d_2 = 0$	$\alpha_2 = 3\pi/2$	$q_{0_2} = 3\pi/2$
$\dot{a}_2 = 0.192$	$\dot{d}_2 = 0.049$	$\dot{\alpha}_2 = 0$	$q'_{0_2} = 0.16$
$a_3 = 0.277$	$d_3 = 0.359$	$\alpha_3 = 0$	$q_{0_3} = 0.16$
$a'_3 = 0.245$	$d'_3 = -0.296$	$\alpha'_3 = 0$	$q'_{0_3} = 1.743$

$\beta = 0.174 \; rad$ (angle of rotation of upper-arm support frame about Y'_2)

*Parameters are found for the reference frames defined in Table 1

$$
\begin{aligned}
\mathbf{T}_{ua}(\boldsymbol{q}) &= \begin{bmatrix} \mathbf{R}_{ua}(\boldsymbol{q}) & \boldsymbol{p}_{ua}(\boldsymbol{q}) \\ 0 & 1 \end{bmatrix}, \\
\mathbf{T}_{la}(\boldsymbol{q}) &= \begin{bmatrix} \mathbf{R}_{la}(\boldsymbol{q}) & \boldsymbol{p}_{la}(\boldsymbol{q}) \\ 0 & 1 \end{bmatrix},
\end{aligned}
\tag{A.1}
$$

where $\boldsymbol{p}_{ua}(\boldsymbol{q}), \boldsymbol{p}_{la}(\boldsymbol{q}) \in \mathbb{R}^3$ are the respective position vectors of the support-frames $\sum_{ua}, \sum_{la}$ in $\sum_0$. $\mathbf{R}_{ua}(\boldsymbol{q}), \mathbf{R}_{la}(\boldsymbol{q}) \in \mathbb{R}^{3 \times 3}$ are the rotation matrices of the respective support-frames $\sum_{ua}, \sum_{la}$ in $\sum_0$.

Jacobian matrices for arm-supports

The current task-space velocities and accelerations of upper and lower-arm supports $\dot{\mathbf{x}}_{ua}, \ddot{\mathbf{x}}_{ua}, \dot{\mathbf{x}}_{la}, \ddot{\mathbf{x}}_{la} \in \mathbb{R}^6$ in the base-frame $\sum_0$ for the given joint velocities and accelerations $\dot{\boldsymbol{q}}, \ddot{\boldsymbol{q}} \in \mathbb{R}^4$ are given by the associated Jacobian $\mathbf{J}_{ua}(\mathbf{q}), \mathbf{J}_{la}(\mathbf{q}) \in \mathbb{R}^{6 \times 4}$ as [47,48]

$$
\begin{aligned}
\dot{\mathbf{x}}_{ua} &= \mathbf{J}_{ua}(\mathbf{q})\dot{\mathbf{q}} = \begin{bmatrix} \dot{\mathbf{x}}_{v_{la}} \\ \dot{\mathbf{x}}_{\omega_{la}} \end{bmatrix} = \begin{bmatrix} \mathbf{J}_{v_{ua}}(\mathbf{q}) \\ \mathbf{J}_{\omega_{ua}}(\mathbf{q}) \end{bmatrix}\dot{\mathbf{q}}, \\
\ddot{\mathbf{x}}_{ua} &= \mathbf{J}_{ua}(\mathbf{q})\ddot{\mathbf{q}} + \dot{\mathbf{J}}_{ua}(\mathbf{q})\dot{\mathbf{q}} = \begin{bmatrix} \ddot{\mathbf{x}}_{v_{ua}} \\ \ddot{\mathbf{x}}_{\omega_{ua}} \end{bmatrix} = \begin{bmatrix} \mathbf{J}_{v_{ua}}(\mathbf{q}) \\ \mathbf{J}_{\omega_{ua}}(\mathbf{q}) \end{bmatrix}\ddot{\mathbf{q}} + \begin{bmatrix} \dot{\mathbf{J}}_{v_{ua}}(\mathbf{q}) \\ \dot{\mathbf{J}}_{\omega_{ua}}(\mathbf{q}) \end{bmatrix}\dot{\mathbf{q}}, \\
\dot{\mathbf{x}}_{la} &= \mathbf{J}_{la}(\mathbf{q})\dot{\mathbf{q}} = \begin{bmatrix} \dot{\mathbf{x}}_{v_{la}} \\ \dot{\mathbf{x}}_{\omega_{la}} \end{bmatrix} = \begin{bmatrix} \mathbf{J}_{v_{la}}(\mathbf{q}) \\ \mathbf{J}_{\omega_{la}}(\mathbf{q}) \end{bmatrix}\dot{\mathbf{q}}, \\
\ddot{\mathbf{x}}_{la} &= \mathbf{J}_{la}(\mathbf{q})\ddot{\mathbf{q}} + \dot{\mathbf{J}}_{la}(\mathbf{q})\dot{\mathbf{q}} = \begin{bmatrix} \ddot{\mathbf{x}}_{v_{la}} \\ \ddot{\mathbf{x}}_{\omega_{la}} \end{bmatrix} = \begin{bmatrix} \mathbf{J}_{v_{la}}(\mathbf{q}) \\ \mathbf{J}_{\omega_{la}}(\mathbf{q}) \end{bmatrix}\ddot{\mathbf{q}} + \begin{bmatrix} \dot{\mathbf{J}}_{v_{la}}(\mathbf{q}) \\ \dot{\mathbf{J}}_{\omega_{la}}(\mathbf{q}) \end{bmatrix}\dot{\mathbf{q}},
\end{aligned}
\tag{A.2}
$$

where $\mathbf{J}_{v_{ua}}(\mathbf{q}), \mathbf{J}_{\omega_{ua}}(\mathbf{q}), \mathbf{J}_{v_{la}}(\mathbf{q}), \mathbf{J}_{\omega_{la}}(\mathbf{q}) \in \mathbb{R}^{3 \times 4}$ are the respective linear and angular velocity Jacobians for the upper and lower-arm support w.r.t base-frame $\sum_0$. Furthermore, $\dot{\mathbf{x}}_{v_{la}}, \dot{\mathbf{x}}_{\omega_{la}}, \dot{\mathbf{x}}_{v_{la}}, \dot{\mathbf{x}}_{\omega_{la}} \in \mathbb{R}^3$ in (A.2) respectively represent the linear and angular components of task-space velocities $\dot{\mathbf{x}}_{ua}, \dot{\mathbf{x}}_{la}$ while $\ddot{\mathbf{x}}_{v_{ua}}, \ddot{\mathbf{x}}_{\omega_{ua}}, \ddot{\mathbf{x}}_{v_{la}}, \ddot{\mathbf{x}}_{\omega_{la}} \in \mathbb{R}^3$ respectively represent the linear and angular components of task-space accelerations $\ddot{\mathbf{x}}_{ua}, \ddot{\mathbf{x}}_{la}$.

If $\mathbf{f}^e_{h_{ua}}$ and $\mathbf{f}^e_{h_{la}} \in \mathbb{R}^6$ are the measured interactive forces on the human at the upper and lower-arm supports in the support-frames $\sum_{ua}, \sum_{la}$ respectively, then the corresponding human interactive joint torques $\boldsymbol{\tau}_{h_{ua}}, \boldsymbol{\tau}_{h_{la}} \in \mathbb{R}^4$ are given by the corresponding end-effector Jacobians $J^e_{ua}(\boldsymbol{q})$, $J^e_{la}(\boldsymbol{q}) \in \mathbb{R}^{6 \times 4}$ as

Table A2
Identified inertial parameters for the 4-ADOF arm exoskeleton *

Properties		Link1	Link 2	Link 3	Link4
Mass (*Kg*)		4.161	3.983	4.571	1.715
Center of Gravity (*m*)		$x_c^{\sum_1}=0.0004$	$x_c^{\sum_2}=-0.0013$	$x_c^{\sum_3}=-0.096$	$x_c^{\sum_{la}}=-0.1249$
		$y_c^{\sum_1}=0.1241$	$y_c^{\sum_2}=-0.0793$	$y_c^{\sum_3}=-0.0149$	$y_c^{\sum_{la}}=-0.0346$
		$z_c^{\sum_1}=0.2031$	$z_c^{\sum_2}=0.2299$	$z_c^{\sum_3}=-0.1435$	$z_c^{\sum_{la}}=0.0630$
Mass Moments of Inertia ($Kg - m^2$)		$I_{xx}^{\sum_1}=0.1470$	$I_{xx}^{\sum_2}=0.11879$	$I_{xx}^{\sum_3}=0.04058$	$I_{xx}^{\sum_{la}}=0.01055$
		$I_{xy}^{\sum_1}=0.00083$	$I_{xy}^{\sum_2}=0.00053$	$I_{xy}^{\sum_3}=-0.00137$	$I_{xy}^{\sum_{la}}=0.00683$
		$I_{xz}^{\sum_1}=-0.0007$	$I_{xz}^{\sum_2}=0.00082$	$I_{xz}^{\sum_3}=-0.00913$	$I_{xz}^{\sum_{la}}=0.00793$
		$I_{yy}^{\sum_1}=0.06973$	$I_{yy}^{\sum_2}=0.09319$	$I_{yy}^{\sum_3}=0.08417$	$I_{yy}^{\sum_{la}}=0.02937$
		$I_{yz}^{\sum_1}=0.05939$	$I_{yz}^{\sum_2}=-0.0426$	$I_{yz}^{\sum_3}=-0.01107$	$I_{yz}^{\sum_{la}}=-0.00343$
		$I_{zz}^{\sum_1}=0.08204$	$I_{zz}^{\sum_2}=0.02987$	$I_{zz}^{\sum_3}=0.06167$	$I_{zz}^{\sum_{la}}=0.02901$

* $\sum_1, \sum_2, \sum_3$ and $\sum_{la}$ are reference frames defined in Table 1

$$\boldsymbol{\tau}_{h_{ua}} = \mathbf{J}^e_{ua}(\mathbf{q})^T \mathbf{f}^e_{h_{ua}} = \begin{bmatrix} \mathbf{J}^{e\ T}_{v_{ua}}(\mathbf{q}) \\ \mathbf{J}^{e\ T}_{\omega_{ua}}(\mathbf{q}) \end{bmatrix} \begin{bmatrix} \mathbf{f}^e_{h_{v_{ua}}} \\ \mathbf{f}^e_{h_{\omega_{ua}}} \end{bmatrix},$$

(A.3)

$$\boldsymbol{\tau}_{h_{la}} = \mathbf{J}^e_{ua}(\mathbf{q})^T \mathbf{f}^e_{h_{ua}} = \begin{bmatrix} \mathbf{J}^{e\ T}_{v_{la}}(\mathbf{q}) \\ \mathbf{J}^{e\ T}_{\omega_{la}}(\mathbf{q}) \end{bmatrix} \begin{bmatrix} \mathbf{f}^e_{h_{v_{la}}} \\ \mathbf{f}^e_{h_{\omega_{la}}} \end{bmatrix},$$

where $\mathbf{J}^e_{v_{ua}}(\mathbf{q}), \mathbf{J}^e_{\omega_{ua}}(\mathbf{q}),\ \mathbf{J}^e_{v_{la}}(\mathbf{q}),\ \mathbf{J}^e_{\omega_{la}}(\mathbf{q}) \in \mathbb{R}^{3 \times 4}$ are respectively the linear and angular-velocity Jacobians for the upper and lower-arm supports w.r.t respective support-frames $\sum_{ua}, \sum_{la}$ respectively. Forces $\mathbf{f}^e_{h_{v_{ua}}}, \mathbf{f}^e_{h_{\omega_{ua}}}, \mathbf{f}^e_{h_{v_{la}}}, \mathbf{f}^e_{h_{\omega_{la}}} \in \mathbb{R}^3$ effectively represent the linear and angular components of the forces $\mathbf{f}^e_{h_{ua}}$ and $\mathbf{f}^e_{h_{la}}$ on human, measured in the respective support-frames $\sum_{ua}$ and $\sum_{la}$.

B. Appendix

Derivation of an impedance control law for a single support 4-ADOF-exoskeleton, using a rigid 6-D force sensor

For a single support 4-ADOF exoskeleton with given joint-space velocities and accelerations $\dot{\mathbf{q}}, \ddot{\mathbf{q}} \in \mathbb{R}^4$, the task-space velocity and acceleration of lower-arm support $\dot{x}_{la}, \ddot{x}_{la} \in \mathbb{R}^6$ are given in terms of linear and angular components in (A.2). The desired task-space velocity and acceleration of the lower-arm support $\dot{\mathbf{x}}_{d_{la}}, \ddot{\mathbf{x}}_{d_{la}} \in \mathbb{R}^6$ can also be similarly defined as

$$\dot{\mathbf{x}}_{d_{la}} = \begin{bmatrix} \dot{\mathbf{x}}_{d_{v_{la}}} \\ \dot{\mathbf{x}}_{d_{\omega_{la}}} \end{bmatrix}, \qquad \ddot{\mathbf{x}}_{d_{la}} = \begin{bmatrix} \ddot{\mathbf{x}}_{d_{v_{la}}} \\ \ddot{\mathbf{x}}_{d_{\omega_{la}}} \end{bmatrix}.$$

(B.1)

The task-space error vectors $\dot{e}_{la}, \ddot{e}_{la} \in \mathbb{R}^6$ for velocity and acceleration are then simply defined from (A.2) as

$$\dot{\mathbf{e}}_{la} = \begin{bmatrix} \dot{\mathbf{e}}_{v_{la}} \\ \dot{\mathbf{e}}_{\omega_{la}} \end{bmatrix} = \dot{\mathbf{x}}_{d_{la}} - \dot{\mathbf{x}}_{la}, \quad \ddot{\mathbf{e}}_{la} = \begin{bmatrix} \ddot{\mathbf{e}}_{v_{la}} \\ \ddot{\mathbf{e}}_{\omega_{la}} \end{bmatrix} = \ddot{\mathbf{x}}_{d_{la}} - \ddot{\mathbf{x}}_{la},$$

(B.2)

where $\dot{\mathbf{e}}_{v_{la}}, \ddot{\mathbf{e}}_{v_{la}} \in \mathbb{R}^3$ are the linear parts of $\dot{e}_{la}$ and $\ddot{e}_{la}$ while $\dot{\mathbf{e}}_{\omega_{la}},\ \ddot{\mathbf{e}}_{\omega_{la}}$ are the corresponding angular parts. Error vectors $\dot{e}_{la}, \ddot{e}_{la}$ are hence straight forward to compute. The linear part of the task-space position error $\mathbf{e}_{v_{la}} \in \mathbb{R}^3$ is also simple to compute and is given by

$$\boldsymbol{e}_{v_{la}} = \boldsymbol{x}_{d_{v_{la}}} - \boldsymbol{x}_{v_{la}},$$

(B.3)

where $\mathbf{x}_{d_{v_{la}}} \in \mathbb{R}^3$ is the desired linear-task-space position of the lower-arm support and $\mathbf{x}_{v_{la}} \in \mathbb{R}^3$ is the corresponding current linear-task-space position which is given from (A.2) as $\mathbf{x}_{v_{la}} = f(\mathbf{T}_{la}(\mathbf{q})) = \mathbf{p}_{la}(\mathbf{q})$.

The angular part of the task-space position error on the other hand, namely $\mathbf{e}_{\omega_{la}} \in \mathbb{R}^3$, is not simple to compute, as the current angular position or the orientation of the lower-arm support in task-space is not given by a vector but in fact by a rotation matrix R_{la} as defined in (A.1). It is though possible to represent the error in orientation $e_{\omega_{la}}$ computationally as a vector by using the axis-angle representation [48]. If $S(\boldsymbol{k})$ is the cross-product operator as defined in [48] then $e_{\omega la}$ can then be written computationally as a vector in terms of the desired and actual rotation matrices of lower-arm support as [48]

$$\mathbf{e}_{\omega_{la}} = \frac{1}{2}\big(\mathbf{S}(\mathbf{n}_{la})\mathbf{n}_{d_{la}} + \mathbf{S}(\mathbf{o}_{la})\mathbf{o}_{d_{la}} + \mathbf{S}(\mathbf{a}_{la})\mathbf{a}_{d_{la}}\big),$$

(B.4)

where $\boldsymbol{n}_{d_{la}}, \boldsymbol{o}_{d_{la}}, \boldsymbol{a}_{d_{la}}$ are the corresponding column vectors of the desired orientation matrix $\mathbf{R}_{d_{la}} \in \mathbb{R}^{3\times3}$ for the lower-arm support. Orientation velocity error $\dot{\mathbf{e}}_{\omega_{la}}$ can then be derived as [48]

$$\dot{\mathbf{e}}_{\omega_{la}} = \mathbf{L}^T \dot{\mathbf{x}}_{d_{\omega_{la}}} - \mathbf{L}\, \dot{\mathbf{x}}_{\omega_{la}},$$

(B.5)

where the matrix $\boldsymbol{L} \in \mathbb{R}^{3x3}$ is defined as

$$\mathbf{L} = \frac{1}{2}\big(\mathbf{S}\big(\mathbf{n}_{d_{la}}\big)\mathbf{S}(\mathbf{n}_{la}) + \mathbf{S}\big(\mathbf{o}_{d_{la}}\big)\mathbf{S}(\mathbf{o}_{la}) + \mathbf{S}\big(\mathbf{a}_{d_{la}}\big)\mathbf{S}(\mathbf{a}_{la})\big).$$

(B.6)

Matrix $\boldsymbol{L}$ in (B.6) is non-singular provided $\boldsymbol{n}_{la}\boldsymbol{n}_{d_{la}} > 0$, $\boldsymbol{o}_{la}\,\boldsymbol{o}_{d_{la}} > 0$, $\boldsymbol{a}_{la}\boldsymbol{a}_{d_{la}} > 0$. Orientation acceleration error $\ddot{\mathbf{e}}_{\omega_{la}}$ can also similarly be written in terms of $\boldsymbol{L}$ as [48]

$$\ddot{\mathbf{e}}_{\omega_{la}} = \mathbf{L}^T \ddot{\mathbf{x}}_{d_{\omega_{la}}} + \dot{\mathbf{L}}^T \dot{\mathbf{x}}_{d_{\omega_{la}}} - \mathbf{L}\, \ddot{\mathbf{x}}_{\omega_{la}} - \dot{\mathbf{L}}\dot{\mathbf{x}}_{\omega_{la}}.$$

(B.7)

If $\mathbf{f}^e_{h_{la}} \in \mathbb{R}^6$ is the measured interactive-force on the human by the 6-D force sensor given in-terms of linear and angular components as defined in (A.3), then the corresponding interactive-force $\mathbf{f}_{h_{la}} \in \mathbb{R}^6$ in the base-frame $\sum_0$ is given in terms of linear and angular components from (A.1) and (A.3) as

$$\mathbf{f}_{h_{la}} = \begin{bmatrix} \mathbf{f}_{h_{v_{la}}} \\ \mathbf{f}_{h_{\omega_{la}}} \end{bmatrix} = \begin{bmatrix} \mathbf{R}_{la}(\mathbf{q}) & 0 \\ 0 & \mathbf{R}_{la}(\mathbf{q}) \end{bmatrix} \begin{bmatrix} \mathbf{f}^e_{h_{v_{la}}} \\ \mathbf{f}^e_{h_{\omega_{la}}} \end{bmatrix}.$$

(B.8)

The linear impedance control law for lower-arm support in terms of $\mathbf{e}_{v_{la}}$ and $\mathbf{f}_{h_{v_{la}}}$ is given from (B.3) and (B.8) as [25]

$$\mathbf{M}_{v_d}\ddot{\mathbf{e}}_{v_{la}} + \mathbf{B}_{v_d}\dot{\mathbf{e}}_{v_{la}} + \mathbf{K}_{v_d}\mathbf{e}_{v_{la}} = \mathbf{f}_{h_{v_{la}}}. \tag{B.9}$$

The reference linear task-space acceleration $\ddot{\mathbf{x}}_{r_{v_{la}}}$ required for ensuring the desired linear-impedance in (B.9) for the lower-arm support is then given from (B.1), (B.2) and (B.3) as

$$\ddot{\mathbf{x}}_{r_{v_{la}}} = \ddot{\mathbf{x}}_{d_{v_{la}}} - \mathbf{M}_{v_d}^{-1}\left(\mathbf{f}_{h_{v_{la}}} - \mathbf{B}_{v_d}\dot{\mathbf{e}}_{v_{la}} - \mathbf{K}_{v_{la}}\mathbf{e}_{v_{la}}\right). \tag{B.10}$$

Where Matrices $\mathbf{M}_{v_d}$, $\mathbf{B}_{v_d}$, $\mathbf{K}_{v_d}$ are the desired linear impedance matrices for mass, damping, and stiffness and are defined as $\mathbf{M}_{v_d} = diag\{m_{v_{d_j}}\}$, $\mathbf{B}_{v_d} = diag\{b_{v_{d_j}}\}$, $\mathbf{K}_{v_d} = diag\{k_{v_{d_j}}\}$. Similarly, the angular-impedance control law for the lower-arm support for computed angular task-space position error $e_{\omega_{la}}$ and the measured task-space angular moment $\mathbf{f}_{h_{\omega_{la}}}$ is given by

$$\mathbf{M}_{\omega_d}\dot{\mathbf{e}}_{\omega_{la}} + \mathbf{B}_{\omega_d}\dot{\mathbf{e}}_{\omega_{la}} + \mathbf{K}_{\omega_d}\mathbf{e}_{\omega_{la}} = \mathbf{f}_{h_{\omega_{la}}}. \tag{B.11}$$

Here $\mathbf{M}_{\omega_d}, \mathbf{B}_{\omega_d}, \mathbf{K}_{\omega_d} \in \mathbb{R}^{3 \times 3}$ are desired angular-impedance matrices for mass, damping, and stiffness and given by $M_{\omega_d} = diag\{m_{\omega_{d_j}}\}$, $\mathbf{B}_{\omega_d} = diag\{b_{\omega_{d_j}}\}$, $\mathbf{K}_{\omega_d} = diag\{k_{\omega_{d_j}}\}$, where $j = 1$ to 3 and $m_{\omega_{d_j}}$, $b_{\omega_{d_j}}$ and $k_{\omega_{d_j}}$ are the respective task-space angular-desired mass, damping, and stiffness parameters. The required reference angular task-space acceleration $\ddot{\mathbf{x}}_{r_{\omega_{la}}}$ for ensuring the desired angular-impedance in (B.11) for the lower-arm support is then given from (B.4), (B.5) and (B.7) as

$$\ddot{\mathbf{x}}_{r_{\omega_{la}}} = \ddot{\mathbf{x}}_{\omega_{la}} - \mathbf{M}_{\omega_d}^{-1}\left(\mathbf{f}_{h_{\omega_{la}}} - \mathbf{B}_{\omega_d}\dot{\mathbf{e}}_{\omega_{la}} - \mathbf{K}_{\omega_d}\mathbf{e}_{\omega_{la}}\right). \tag{B.12}$$

The reference task-space acceleration for lower-arm support $\ddot{\mathbf{x}}_{r_{la}} \in \mathbb{R}^6$ can be written as linear and angular components from (B.10) and (B.12) as

$$\ddot{\mathbf{x}}_{la} = \begin{bmatrix} \ddot{\mathbf{x}}_{r_{v_{la}}} \\ \ddot{\mathbf{x}}_{r_{\omega_{la}}} \end{bmatrix}. \tag{B.13}$$

The corresponding reference joint-space acceleration $\ddot{\mathbf{q}}_r \in \mathbb{R}^4$ is then given in terms of the lower-arm support Jacobian from (A.2) and (B.13) as an overdetermined least square solution,

$$\ddot{\mathbf{q}}_r = \mathbf{J}_{la}(\mathbf{q})^{+}\left(\ddot{\mathbf{x}}_{r_{la}} - \dot{\mathbf{J}}_{la}(\mathbf{q})\dot{\mathbf{q}}\right). \tag{B.14}$$

$J_{la}(q)^{+} \in \mathbb{R}^{4x6}$ in (B.14) represents the pseudo inverse of $J_{la}(q)$.

C. Appendix

The transfer functions $g_{A_n}(s)_j$ and $g_{B_n}(s)_j$ defined in (11) are defined in terms of the nominal parameters of the CCDC-drive, listed in Table C1–Table C3 as

$$g_{A_n}(s)_j = \frac{g_c(s)_j\, g_r(s)_j\, g_{zoh}(s)_j}{d_f(s)_j}, \quad g_{B_n}(s)_j = g_D(s)_j + g_2(s)_j,$$

$$where$$

$$g_D(s)_j = \frac{h_{cj}\, g_c(s)_j\, g_t(s)_j\, g_r(s)_j}{d_f(s)_j},$$

$$d_f(s)_j = \left(1 + h_{c_j}\, g_c(s)_j\, g_r(s)_j\, g_a(s)_j\right)$$

$$g_2(s)_j = \frac{k_{n_j}}{\left(1 + \tau_{n_j}\, s\right)\left(1 - k_{t_j}\, g_\tau(s)_j\right)}, \tag{C.1}$$

$$g_\tau(s)_j = \frac{k_{a_j}k_{b_j}\, k_{n_j}}{d(s)_j},$$

$$d(s)_j = \left(1 + \tau_{a_j}s\right)\left(1 + \tau_{n_j}s\right) + k_{a_j}\, k_{b_j}\, k_{t_j}\, k_{n_j},$$

$$for\ j = 1\ to\ 4$$

An explicit expression for $n_D c(s)_j$ defined in (12) is found in terms of the nominal parameters of the CCDC-drive, listed in Table C-1-Table C-3 as

$$n_{Dc}(s)_j = \left[\begin{array}{c} t_s\tau_{a_j}t_{r_j}s^4 + \left(2t_s\tau_{a_j} + t_st_{r_j} + 2\tau_{a_j}t_{r_j}\right)s^3 + \\ \left(2t_s + 4\tau_{a_j} + 2t_{r_j}\right)s^2 + \left(2t_sh_{c_j}k_{c_j}k_{r_j}k_{a_j} + 4\right)s + 4h_{c_j}k_{c_j}k_{r_j}k_{a_j} \end{array}\right] \Bigg/ \left(k_{c_j}k_{r_j}k_{a_j}k_{t_j}\right), \tag{C.2}$$

for $j = 1$ to 4. The transfer functions $g_{T_n}(s)_j$ defined in (15) is defined in terms of the nominal parameters of the CCDC-drive, listed in Table C-1-Table C-3 as

Table C1
Independent parameters for the j_{th} CCDC-drive

Symbol	Quantity
r_{a_j}	Armature resistance
l_{a_j}	Armature inductance
k_{s_j}	Motor speed constant
$i_{a_{max_j}}$	Maximum continuous current
j_{m_j}	Motor rotor inertia
$\dot{q}_{max_j}$	Maximum rotor velocity
i_{o_j}	Motor no-load current
k_{t_j}	Motor torque constant
j_{g_j}	Gear moment of inertia
f_{g_j}	Gear viscous friction coefficient
η_j	Gear ratio
t_s	Sampling time
$\tau_{L_{m_j}}$	Motor load-torque
$\tau_{L_{m_{R_j}}}$	Rated motor load-torque

Table C2
Dependent parameters for the j_{th} CCDC-drive

Symbol	Quantity	Relationship
k_{a_j}	Electrical gain	$1/r_{a_j}$
τ_{a_j}	Electrical time constant	l_{a_j}/r_{a_j}
k_{b_j}	Back EMF constant	$1/k_{s_j}$
τ_{f_j}	Motor viscous friction torque	$(i_{o_j} k_{t_j})$
f_{m_j}	Motor viscous friction coefficient	$\tau_{f_j}/\dot{q}_{max_j}$
k_{m_j}	Motor mechanical gain	$1/f_{m_j}$
τ_{m_j}	Motor mechanical time constant	$(k_{m_j} j_{m_j})$
f_{n_j}	Net viscous friction coefficient	$(f_{m_j} + f_{g_j}/(\eta_j)^2)$
j_{n_j}	Net moment of inertia	$(j_{m_j} + j_{g_j}/(\eta_j)^2)$
k_{n_j}	Net mechanical gain	$1/f_{n_j}$
τ_{n_j}	Net mechanical time constant	$(k_{n_j} j_{n_j})$

Table C3
Parameters for PWM Converter for the j_{th} CCDC-drive

Symbol	Quantity
f_{c_j}	Converter switching frequency
t_{r_j}	Converter sample time $= 1/f_{c_j}$
V_{dc_j}	Converter input DC voltage
$v_{c_{max_j}}$	Maximum control voltage
k_{r_j}	Converter gain
$i_{a_{max_j}}$	Maximum armature current
$i_{s_{max_j}}$	Maximum sensed current
h_{c_j}	Current feedback gain
k_{c_j}	Current controller gain

Table C4
Selected actuator specifications for each joint.

Joint angle	DC motor	Gear head	Encoder (lines/turn)	Output-shaft rated torque (Nm)	Range of q_i (degrees)
q_1	24V	43	1024	18 Nm	10° to 120°
q_2	48V	81	1600	40-Nm	240° to 350°
q_3	48V	81	1600	40-Nm	-45° to 140°
q_4	24V	43	1024	18 Nm	10° to 150°

$$g_{T_n}(s)_j = g'_{A_n}(s)_j \frac{h_{c_j}}{k_{t_j}},$$

where

$$g'_{A_n}(s)_j = \frac{k_{A_j}}{(1 + \tau_{A_j}s)}, \qquad k_{A_j} = \frac{k_{t_j} k_{n_j}}{h_{c_j}}, \tag{C.3}$$

$$\tau_{A_j} = \frac{a_j + h_{c_j}k_{c_j}\tau_{n_j}k_{a_j}k_{r_j}}{h_{c_j}k_{c_j}\tau_{n_j}k_{a_j}k_{r_j}}, \qquad a_j = 1 + k_{a_j} \ k_{b_j} \ k_{t_j} \ k_{n_j},$$

for $j = 1$ to 4

References

[1] Gopura RARC, Kiguchi K, Li Y. SUEFUL-7: A 7DOF upper-limb exoskeleton robot with muscle-model-oriented EMG-based control. Proc. of 2009 IEEE/RSJ Int. Conf. Intell. Robots Syst. 2009:1126–31. Oct.

[2] Kim B, Deshpande AD. An upper-body rehabilitation exoskeleton harmony with an anatomical shoulder mechanism: Design, modeling, control, and performance evaluation. Int. J. Robot. Res. 2017;36(4):414–35.

[3] Perry JC, Rosen J, Burns S. Upper-limb powered exoskeleton design. IEEE/ASME Trans. Mechatronics 2007;12(4):408–17. Aug.

[4] Rahman M, Rahman M, Christobal O, Saad M, Kenne J, Archambault P. Development of a whole arm wearable robotic exoskeleton for rehabilitation and to assist upper limb movements. Robotica 2015;33:19–39. Jan.

[5] Nef T, Mihelj M, Kiefer G, Riener R. ARMin exoskeleton for arm therapy in stroke patients. Proc. of 2007 IEEE 10th Int. Conf. Rehabil. Robot. 2007:68–74. Jun.

[6] Ren Y, Park HS, Zhang LQ. Developing a whole-arm exoskeleton robot with hand opening and closing mechanism for upper limb stroke rehabilitation. Proc. IEEE 11th Int. Conf. Rehabil. Robot. 2009:761–5. Jun.

[7] Mallwitz M, Niels W, Teiwes J, Kirchner EA. The capio active upper body exoskeleton and its application for teleoperation. Proc. of 13th Symposium on Advanced Space Technology in Robotics and Automation, Noordwijk 2015. May.

[8] Rahman M, Saad M, Kenné J, Archambault P. Exoskeleton robot for rehabilitation of elbow and forearm movements. Proc. 18th Mediterranean Conf. Control Autom. 2010:1567–72. Jun.

[9] Gupta and M. K. Design of a haptic arm exoskeleton for training and rehabilitation. IEEE/ASME Trans. Mechatronics 2006;11(3):280–9. Jun.

[10] Bai S, Christensen S, Islam MR. An upper-body exoskeleton with a novel shoulder mechanism for assistive applications. Proc. 2017 IEEE Int. Conf. Adv. Intell. Mechatronics 2017:1041–6. July.

[11] Garrec P, Friconneau J, Méasson Y, Perrot Y. ABLE, an innovative transparent exoskeleton for the upper-limb. Proc. 2008 IEEE/RSJ Int. Conf. Intell. Robots Syst. 2008:1483–8. Sep.

[12] Nef T, Guidali M, Riener R. ARMin III – Arm therapy exoskeleton with an ergonomic shoulder actuation. Appl. Bionics Biomech. 2009;6(2):127–42. Jun.

[13] Frisoli FSalsedo, Bergamas M. A Force-feedback exoskeleton for upper-limb rehabilitation in virtual reality. Appl. Bionics Biomech. 2009;6(2):115–26. Jun.

[14] Balasubramanian S, Wei R, Perez M, Shepard B, Koeneman E, Koeneman J, He J. RUPERT: An exoskeleton robot for assisting rehabilitation of arm functions. 2008 Virtual Rehabil. 2008:163–7. Aug.

[15] Otsuka T, Kawaguchi K, Kawamoto H, Sankai Y. Development of upper-limb type HAL and reaching movement for meal-assistance. Proc. 2011 IEEE Int. Conf. Robot. Biomimetics 2011:883–8. Dec.

[16] Robinson DW. Design and analysis of series elasticity in closed-loop actuator force control. Massachusetts: Massachusetts Institute of Technology; 2000. Jun. 2000.

[17] van der Kooij H, Veneman J, Ekkelenkamp R. Compliant actuation of exoskeletons. Mobile Robots: Towards New Applications. Rijeka: IntechOpen; 2006. p. 129–48. Dec.

[18] M. D. Taylor , "A compact series elastic actuator for bipedal robots with human-like dynamic performance," Aug.2011.

[19] Vantilt J, Tanghe K, Afschrift M, Bruijnes AKBD, Junius K, Geeroms J, Aertbeliën E, De Groote F, Lefeber D, Jonkers I, De Schutter J. Model-based control for exoskeletons with series elastic actuators evaluated on sit-to-stand movements. J. Neuroeng. Rehabil. 2019;16(1):65.

[20] Kong K, Bae J, Tomizuka M. A compact rotary series elastic actuator for human assistive systems. IEEE/ASME Trans. Mechatronics 2012;17(2):288–97. Apr.

[21] Vallery H, Veneman J, Asseldonk EV, Buss M. Compliant actuation of rehabilitation robots. IEEE Robot. Autom. Mag. 2008:60–8. Sep.

[22] dos Santos WM, Siqueira AA. Impedance control of a rotary series elastic actuator for knee rehabilitation. Proc. 19th World Congress: Int. Feder. Autom. Control 2014:4801–6. Aug.

[23] Colgate J, Hogan N. Robust control of dynamically interacting systems. Int. J. Control 1988;48(1):65–88.

[24] Lawrence D. Impedance control stability properties in common implementation. Proc. 1988 IEEE Int. Conf. Robot. Autom. 1988;2:1185–90. Apr.

[25] Hogan N. Impedance control : An approach to manipulation. ASME J. Dyn. Syst. Meas. Control 1985;107(1):1–24. Mar.

[26] Sadeghian H, Villani L, Keshmiri M, Siciliano B. Task-space control of robot manipulators with null-space compliance. IEEE Trans. Robot. 2014;30(2):493–506. Apr.

[27] Platt Jr R, Abdallah M, Wampler C. Multiple-priority impedance control. Proc. IEEE Int. Conf. Robot. Autom. 2011:6033–8.

[28] Huang Z, Liu J, Li Z, Su C. Adaptive impedance control of robotic exoskeletons using reinforcement learning. Proc Int. Conf. Adv. Robot. Mechatronics 2016: 243–8.

[29] Ollinger GA, Colgate JE, Peshkin MA, Goswami A. Active-impedance control of a lower-limb assistive exoskeleton. Proc. 2007 IEEE 10th Int. Conf. Rehabil. Robot. 2007:188–95.

[30] Wang J, Li Y. Hybrid impedance control of a 3-DOF robotic arm used for rehabilitation treatment. Proc. 6th Annual IEEE Conf. Autom Sci. Eng. 2010: 768–73. Aug.

[31] Lee H, Lee B, Kim W, Gil M, Han J, Han C. Human-robot cooperative control based on pHRI of exoskeleton robot for a human upper extremity. Int. J. Precis. Eng. Manuf. 2012;13(6):985–92. Jun.

[32] Yu W, Rosen J, Li X. PID admittance control for an upper limb exoskeleton. Proc. of 2011 American Control Conf 2011:1124–9.

[33] Maggioni S, Reinert N, Lünenburger L, Melendez-Calderon A. An adaptive and hybrid end-point/joint impedance controller for lower limb exoskeletons. Frontiers in Robotics and AI 2018;5:104.

[34] Masud N, Smith C, Isaksson M. Disturbance observer based dynamic load torque compensator for assistive exoskeleton. Mechatronics 2018;54:78–93. Oct.

[35] Jarrasse N, Morel G. Connecting a human limb to an exoskeleton. IEEE Trans. Robot. 2012;28(3):697–709. Jun.

[36] Hogan N, Buerger SP. Impedance and interaction control. Robotics and Automation Handbook. CRC-Press; 2004. p. 19.1–19.24.

[37] Shaari N, Md Isa I, Jun T. Torque analysis of lower limb exoskelton robot design. ARPN J. Eng. Appl. Sci. 2015;10(19):9141–9. Oct.

[38] Krishnan R. Electric Motor Drives: Modeling Analysis and Control. New Jersey: Prentice Hall; 2001.

[39] Kang SH, Jin M, Chang PH. A solution to the accuracy/robustness dilemma in impedance control. IEEE Trans. Mechtronics 2009;14(3):282–94.

[40] Mosadeghzad M, Medrano-Cerda G, Saglia J, Tsagarakis NG, Caldwell D. Comparison of various active impedance control approaches: Modeling, implementation, passivity, stability and trade-offs. Proc. 2012 IEEE/ASME Int. Conf. Adv. Intell. Mechatronics 2012:342–8. Jul.

[41] NASA, "Man system integration standards, Vol. 1, Sec. 3," NASA, [Online]. Available: https://msis.jsc.nasa.gov/sections/section03.htm. [Accessed 15 1 2019].

[42] Rosen J, Perry JC, Manning N, Burns S, Hannaford B. The human arm kinematics and dynamics during daily activities – toward a 7 DOF upper limb powered exoskeleton. Proc.12th Int. Conf. Adv. Robot. 2005:532–9. July.

[43] Artemiadis PK, Katsiaris PT, Liarokapis MV, Kyriakopoulos KJ. Human arm impedance: Characterization and modeling in 3D space. Proc. IEEE/RSJ Int. Conf. Intell. Robots Syst. 2010:3103–8.

[44] Jacopo B, Giancarlo F, Joost J, Elena DM. On the value of estimating human arm stiffness during virtual teleoperation with robotic manipulators. Frontiers in Neuroscience 2017;11:528.

[45] Dimeas F, Aspragathos N. Online stability in human-robot cooperation. IEEE Trans. Haptics 2016;9(2):267–78. June.

[46] An C, Hollerbach J. Dynamic stability issues in force control of manipulators. Proc. 1987 IEEE Int. Conf. Robot. Autom. 1987:890–6. April.

[47] Spong MW, Hutchinson S, Vidyasagar M. Robotic Dynamics and Control. John Wiley And Sons; 2004.

[48] Lewis FL, Dawson DM, Abdallah CT. Robot Manipulator Control Theory and Practice,Second Edition. New York: Marcel Dekker; 2004.

Nauman Masud is currently working at Department of Electrical Engineering, Mathematics and Science, University of Gävle, Sweden and he is a registered PhD student at Robotics, Perception, and Learning Laboratory at The Royal Institute of Technology Stockholm, Sweden (KTH). He received his B.Sc. Electrical Engineering degree of University of Engineering and Technology Peshawar, Pakistan. He received his M.Sc. System Engineering from Quaid-e-Azam University Islamabad, Pakistan. His current research interests include modeling and control of assistive exoskeletons, human-robot interaction and real time control of electromechanical systems.

Dario Senkic is a Lab Engineer at Department of Industrial Design, Industrial Management and Mechanical Engineering, University of Gävle. He received his B.Sc. Engineering degree in Automation and Manufacturing from the University of Gävle, Sweden in 2014. His research interests include mechanical design and manufacturing of assistive exoskeletons, engine design, and CNC based automated manufacturing.

Christian Smith is an Assistant Professor in Computer Science at the Robotics, Perception, and Learning Laboratory at The Royal Institute of Technology in Stockholm (KTH). He received his M.Sc. in Engineering Physics in 2005, and Ph.D. in Computer Science in 2009, both at KTH. He has been a postdoctoral researcher at Advanced Telecommunications Research International (ATR) in Kyoto, Japan. He is the secretary of the IEEE Robotics and Automation Society Swedish Chapter. Research interests include control and modelling for manipulation and grasping in human-centric environments and human–robot interaction.

Magnus Isaksson is a Professor, Department Head and the Head of Research at Department of Electrical Engineering, Mathematics and Sciences, University of Gävle. He received his M.Sc. degree in microwave engineering from the University of Gävle, Sweden, in 2000. The Licentiate degree from Uppsala University, Uppsala, Sweden, in 2006, and the Ph.D. degree from the KTH Royal Institute of Technology, Stockholm, Sweden, in 2007. In 2012, he was a Docent with the KTH Royal Institute of Technology. His current research interests include compensation of nonlinear modelling and characterization of devices and systems, signal processing, and assistive exoskeletons.